Diffuse Deformation and Surface Faulting Distribution from Submetric Image Correlation along the 2019 Ridgecrest, California, Ruptures

Solène L. Antoine*[1], Yann Klinger[1], Arthur Delorme[1], Kang Wang[2], Roland Bürgmann[2], and Ryan D. Gold[3]

ABSTRACT

The 2019 M_w 6.4 and 7.1 Ridgecrest, California, earthquake sequence (July 2019) ruptured consecutively a system of high-angle strike-slip cross faults (northeast- and northwest-trending) within 34 hr. The complex rupture mechanism was illuminated by seismological and geodetic data, bringing forward the issue of the interdependency of the two fault systems both at depth and at the surface, and of its effect on the final surface displacement pattern. Here, we use high-resolution (WorldView and Pleiades) optical satellite image correlation to measure the near-fault horizontal and vertical surface displacement fields at 0.5 m ground resolution for the two earthquakes. We point out significant differences with previous geodetic- and geologic-based measurements, and document the essential role of distributed faulting and diffuse deformation in producing the observed surface displacement patterns. We derive strain fields from the horizontal displacement maps, and highlight the predominant role of rotation and shear strain in the surface rupture process. We discuss the segmentation of the rupture based on the fault geometry and along-strike slip variations. We also image several northeast-trending faults with similar orientation to the deeply embedded shear fabric identified in aftershock studies, and show that these cross faults are present all along the rupture, including at a scale < 100 m. Finally, we compare our results to kinematic slip inversions, and show that the surface diffuse deformation is primarily associated with areas of shallow slip deficit; however, this diffuse deformation cannot be explained using elastic modeling. We conclude that inelastic processes play an important role in contributing to the total surface deformation associated with the 2019 Ridgecrest sequence.

KEY POINTS

- East–west, north–south, and vertical surface displacement maps are calculated at 0.5 m ground resolution.
- We separate contributions from localized slip on faults and diffuse deformation in the surrounding medium.
- We show the contribution of inelastic deformation to surface diffuse deformation.

Supplemental Material

INTRODUCTION

Geometrical complexity of earthquake surface ruptures has been described for a wide range of fault systems over the last decades based on geological (e.g., Tchalenko and Ambraseys, 1970; Klinger *et al.*, 2005; Mitchell and Faulkner, 2009; Griffith *et al.*, 2010; Choi *et al.*, 2018) and geodetic observations (e.g., Milliner *et al.*, 2015; Vallage *et al.*, 2015, 2016; Delorme *et al.*, 2020). Numerical approaches also enable us to establish a relation between observations of fault-zone complexity and the mechanical and physical properties of the fault itself (e.g., Finzi and Langer, 2012; Klinger *et al.*, 2018). The combination of these different observations suggests a relationship between the fault geometry and the lateral extent of a coseismic rupture. The term "fault segmentation" is used to describe the laterally discontinuous fault geometry and the control these discontinuities exert on the propagation of the rupture. For example, changes in the fault scarp morphology and fault

1. Université de Paris, Institut de physique du globe de Paris, CNRS, Paris, France, https://orcid.org/0000-0002-5663-7292 (SLA); https://orcid.org/0000-0003-2119-6391 (YK); https://orcid.org/0000-0002-7141-6148 (AD); 2. Department of Earth and Planetary Sciences, University of California, Berkeley, Berkeley, California, U.S.A., https://orcid.org/0000-0002-9725-3295 (KW); https://orcid.org/0000-0002-3560-044X (RB); 3. U.S. Geological Survey, Geologic Hazards Science Center, Golden, Colorado, U.S.A., https://orcid.org/0000-0002-4464-6394 (RDG)

*Corresponding author: santoine@ipgp.fr

Cite this article as Antoine, S. L., Y. Klinger, A. Delorme, K. Wang, R. Bürgmann, and R. D. Gold (2021). Diffuse Deformation and Surface Faulting Distribution from Submetric Image Correlation along the 2019 Ridgecrest, California, Ruptures, *Bull. Seismol. Soc. Am.* **XX**, 1–28, doi: 10.1785/0120210036

geometry combined with lateral variations in the recurrence intervals of past earthquakes along the Wasatch normal fault (Utah, United States, 370 km long) have enabled identification of individual fault segments that behave differently (Schwartz and Coppersmith, 1984; DuRoss *et al.*, 2016). These variations also coincide with changes in the trend of the fault that often are separated by prominent fault structural complexities (Schwartz and Coppersmith, 1984). Segmentation of fault systems is also widely observed in strike-slip contexts, for example, the 2001 Kokoxili earthquake in central Tibet or the 1905 $M_w > 8$ Tsetserleg-Bunlay earthquake in Mongolia. Using satellite optical imagery-based measurements, Klinger *et al.* (2006) and Choi *et al.* (2018) described the segmentation of these two ruptures, respectively; they identified a decrease in surface fault slip every ~20 km along the rupture, which corresponds to the location of fault bends and stepovers. They conclude that large earthquakes are generated by the rupture of multiple fault segments, separated from each other by geometrical barriers.

Geometrical barriers are important features, because they represent either stopping or favorable initiating points for earthquake ruptures, depending on local stress conditions (King and Nabelek, 1985; Klinger *et al.*, 2006; Finzi and Langer, 2012; Lozos *et al.*, 2012; Biasi and Wesnousky, 2017). At these locations, surface displacements can be particularly difficult to characterize and to quantify, because part of the slip is distributed in the surrounding medium through secondary faulting and diffuse deformation (Klinger *et al.*, 2006; Gold *et al.*, 2015; Zhou *et al.*, 2018). This occurs principally around the major geometrical barriers, although it can also be observed to a lesser extent at every geometrical complexity along any surface rupture (Milliner *et al.*, 2015; Milliner, Sammis, *et al.*, 2016).

In this study, the term "localized deformation" characterizes slip that occurs on an actual fault of either primary or secondary strands. Conversely, "diffuse deformation" is used to describe any type of deformation, elastic and inelastic, characterized by large-scale displacement gradients in the bulk medium, without surface rupturing. Near-fault diffuse deformation generally arises from the bulk response to subsurface variations of slip on the fault, including shallow slip deficit (SSD; Fialko *et al.*, 2005; Brooks *et al.*, 2017; Nevitt *et al.*, 2020). It is encountered at all spatial scales, and the contribution to the total surface displacement pattern remains poorly understood. Inelastic diffuse deformation regroups any deformation apart from elastic processes. The current understanding of processes that accommodate inelastic diffuse deformation include block rotations (McGill and Rubin, 1999; Shelef and Oskin, 2010), microscale brittle deformations (McGill and Rubin, 1999; Hamiel *et al.*, 2004), and granular flow (Hamiel *et al.*, 2004; Fossen *et al.*, 2007). We note that the definition of diffuse deformation used in this study refers to large-scale (>500 m) gradients of displacement. It differs from the more commonly used definition of off-fault deformation (OFD), which is inferred from the difference between fault offsets measured using satellite imagery analysis over a limited aperture of a couple hundred meters, and that measured on discrete faults in the field (Zinke *et al.*, 2014; Milliner *et al.*, 2015, 2021; Gold *et al.*, 2021).

Earthquake sequences involving cross faults (Hudnut *et al.*, 1989; Kilb and Rubin, 2002), such as the 2019 Ridgecrest sequence, generate particularly complex surface ruptures since two sets of faults at high angles to one another accommodate the earthquake deformation. Thus, high-resolution data that describe the surface displacement distribution are crucial to characterize the slip on the different faults that ruptured, the geometrical relations between the faults, and the way faults (primary and secondary) as well as zones of diffuse deformation contribute to the total earthquake displacement budget. Key questions about this earthquake sequence include the role of the two different sets of faults in the earthquake mechanisms, and how interactions between the primary fault system and the cross faults influenced the coseismic surface displacement budget and deformation patterns.

In the following, we document, analyze, and discuss near-fault surface displacement patterns for the 2019 Ridgecrest earthquake sequence. We first describe the context of the earthquake sequence, including the M_w 6.4 foreshock and the M_w 7.1 mainshock, and we review the different observations and measurements already available. Next, we detail the optical image-correlation methodology used to measure the 3D surface displacement field associated with the earthquake rupture sequence, and we describe the results obtained. We then extract slip values from the displacement maps across the entire fault-zone width (FZW) and measure the slip distribution in the parallel, perpendicular, and vertical components of the deformation. We also discriminate between the contributions of localized slip on discrete faults and diffuse deformation occurring in the surrounding medium. Finally, we compare these results with previously published kinematic inversions and subsurface fault geometries inferred from relocated aftershocks to relate earthquake process at depth with patterns of surface displacement we have observed.

THE RIDGECREST EARTHQUAKE SEQUENCE

The 2019 Ridgecrest earthquakes (M_w 6.4 and 7.1), referred to as the Ridgecrest sequence, occurred during 4–6 July 2019 in southern California. The two events are located at the transition between the southern Walker Lane and the eastern California shear zone (Fig. 1). The southern Walker Lane and eastern California shear zone are part of a system of distributed faulting that accommodates 20% of the relative dextral motion between the Pacific and North America plates (Carlson *et al.*, 2013). Three large historical earthquakes that occurred within this region include the 1872 M_w 7.7 Owens Valley (Haddon *et al.*, 2016), 1992 M_w 7.3 Landers (Massonnet *et al.*, 1993; Sieh *et al.*, 1993), and 1999 M_w 7.1 Hector Mine earthquakes (Fialko *et al.*, 2001; Treiman *et al.*, 2002). The Ridgecrest

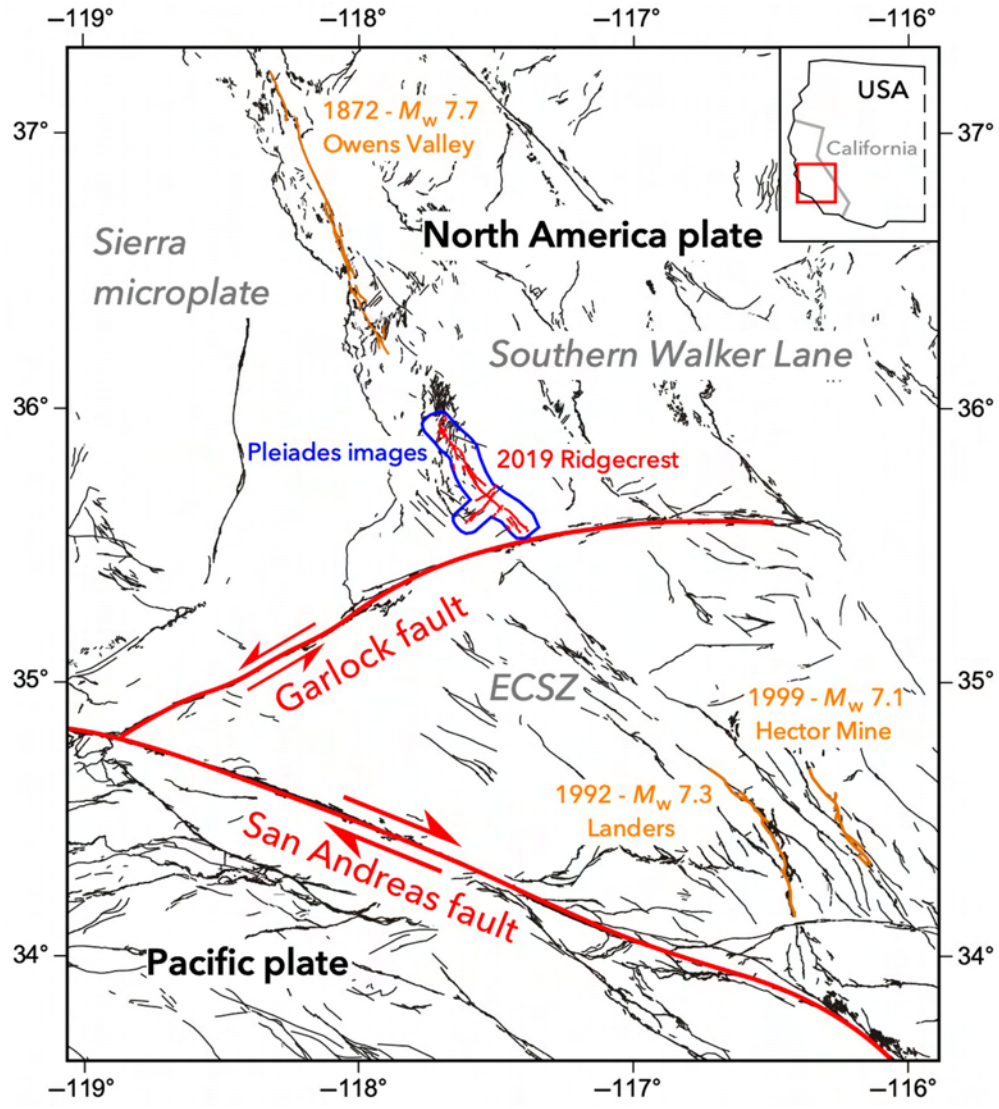

Figure 1. Tectonic context of the Ridgecrest sequence. Pacific plate relative motion to North America plate is 49 mm/yr (ten Brink *et al.*, 2018). ECSZ stands for eastern California shear zone. Quaternary faults (U.S. Geological Survey [USGS] database; see Data and Resources.) are shown in black. Major faults, including the Garlock and San Andreas faults, and the 2019 Ridgecrest surface ruptures are highlighted in red. Large historical earthquake ruptures are shown in orange (Haddon *et al.*, 2016; Milliner, Dolan, *et al.*, 2016). The blue polygon around the Ridgecrest earthquake shows the area covered by the postearthquake, high-resolution Pleiades images (Table S1). Inset map shows the location of the western USA. The color version of this figure is available only in the electronic edition.

sequence was unexpected, because it occurred on a system of faults that was not identified as potential active faults. However, retrospective analysis of high-resolution topography data has revealed structures predating the 2019 ruptures (Jobe *et al.*, 2020). The M_w 7.1 mainshock rupture southeastern end is located just a few kilometers north of the sinistral Garlock fault, which is a major active fault in southern California. After the 2019 Ridgecrest sequence, surface creep (Ross *et al.*, 2019; Barnhart *et al.*, 2020) as well as clusters of seismicity (Shelly, 2020) were triggered on a section of the Garlock fault, which has not ruptured in the last thousand years (with the exception of an M_w 5.7 earthquake recorded in 1992, which was probably triggered by the Landers earthquake; Petersen and Wesnousky, 1994; Dolan *et al.*, 2016). Therefore, the occurrence of the 2019 Ridgecrest earthquake sequence and its triggering activities on the Garlock fault raise concerns about future seismic hazard in this area of southern California.

The M_w 6.4 and 7.1 events of the Ridgecrest sequence ruptured consecutively a system of high-angle strike-slip cross faults (northeast- and northwest-trending) within 34 hr. The first-order geometry of the ruptures was highlighted by seismological data (e.g., Ross *et al.*, 2019; Shelly, 2020) and surface observations (e.g., DuRoss *et al.*, 2020; Milliner and Donnellan, 2020; Ponti *et al.*, 2020). The first earthquake of magnitude M_w 6.4 occurred on 4 July 2019. Although it initiated on a northwest-striking fault, it mainly ruptured a set of northeast-trending left-lateral faults extending for 15 km (Ross *et al.*, 2019; Huang *et al.*, 2020; Milliner and Donnellan, 2020; Wang *et al.*, 2020). This event is referred to as the foreshock of the sequence. The M_w 7.1 mainshock occurred on 6 July 2019 and ruptured a northwest-trending set of right-lateral faults for 50 km (Ross *et al.*, 2019; Milliner and Donnellan, 2020). Inversions of geodetic and seismological data (e.g., Chen *et al.*, 2020; Jin and Fialko, 2020; Qiu *et al.*, 2020; Wang *et al.*, 2020; Xu *et al.*, 2020), optical imagery (Barnhart *et al.*, 2020; Milliner and Donnellan, 2020; Milliner *et al.*, 2021), and field-based measurements (DuRoss *et al.*, 2020; Ponti *et al.*, 2020) indicate a maximum of 1.5–2 m of left-lateral slip for the foreshock and 5–6 m of right-lateral slip for the mainshock. Coseismic slip and aftershocks are limited to the upper ~15 km of the seismogenic crust (Ross *et al.*, 2019; Cheng and Ben-Zion, 2020; Huang *et al.*, 2020; Shelly, 2020). At the surface, the ruptures

cut through young alluvium and Quaternary lake and playa deposits, as well as bedrock outcrops of Mesozoic granite (Jennings *et al.*, 1962; DuRoss *et al.*, 2020; Zimmaro *et al.*, 2020).

DATA AND METHODS

To characterize and quantify the surface displacements associated with the Ridgecrest earthquakes, we used a series of high-resolution (0.5 m) optical images that were acquired before and after the earthquake sequence by the WorldView and Pleiades satellites (Table S1, available in the supplemental material to this article.). The pre-earthquake images are a combination of archived mono-images from the WorldView and Pleiades satellites acquired between May 2012 and June 2018 (Table S1). No major earthquake ($M_w > 5$) occurred in this area since the 1995 Ridgecrest sequence (Hauksson *et al.*, 1995), and the interseismic strain rate in this area is relatively low, as indicated by Global Navigation Satellite Systems (GNSS) and Interferometric Synthetic Aperture Radar (InSAR) measurements (e.g., Gan *et al.*, 2000; Peltzer *et al.*, 2001). Thus, images spanning 2012–2018 can be used safely as reference for the pre-earthquake period. The postearthquake dataset includes tri-stereo Pleiades images with three different acquisitions covering the northwestern, the center, and the southeastern parts of the rupture (Table S1). Those images were acquired ~1.5 month after the earthquakes, over a span of 20 days. Postseismic deformation for the two months period after the earthquake series is estimated to be about 5 cm in the line of sight of Sentinel-2 satellites (Brooks *et al.*, 2020; Wang and Bürgmann, 2020); therefore, the surface displacements derived in this study likely include limited postseismic deformation of a few centimeters. Because there was no stereo (or tri-stereo) image acquisition with <0.5 m resolution between the two earthquakes of the 2019 sequence, our measurements combine surface displacements associated with both the mainshock and the foreshock earthquakes, as well as approximately two months of postseismic deformation. Milliner and Donnellan (2020) used 3 m resolution Planet Labs satellite images collected on a daily basis to separate surface faulting from the two events. This enables us to assume that the northeast-trending surface rupture is associated with the foreshock earthquake, whereas the northwest-trending surface rupture occurred during the mainshock earthquake (Ross *et al.*, 2019; Barnhart *et al.*, 2020). To image the whole area of the Ridgecrest surface rupture, we used 14 combinations of pre-earthquake and postearthquake images, referred to as tiles (Fig. S1 and Table S2). The image processing described later was performed independently on the 14 tiles, which were subsequently mosaicked to obtain a continuous displacement map.

To obtain the horizontal displacement field, we performed subpixel cross correlation between the sets of pre-earthquake and postearthquake images using the MicMac package (Rosu *et al.*, 2015; Rupnik *et al.*, 2016, 2017). This method preserves the input image resolution of 0.5 m through the correlation process and allows us to measure surface displacements with a detection threshold down to 5 cm (approximately one-tenth of the image resolution) for the most favorable signal-to-noise ratios (Rosu *et al.*, 2015; Delorme *et al.*, 2020). Prior to correlation, to correct for distortions related to variable viewing angles and topography, each image was orthorectified using a digital surface model (DSM) with a resolution consistent with the images. Independent DSMs for the pre-earthquake and postearthquake scenes were used to avoid orthorectification errors due to the coseismic displacement between the pre-earthquake and postearthquake image acquisitions.

For the pre-earthquake dataset, we ran image orthorectification with two different pre-earthquake DSMs. We compared the correlation results obtained with the two methods for each image tile, and we kept the results showing lower orthorectification artifacts (Fig. S2). On the one hand, using MicMac, we calculated a 0.5 m resolution pre-earthquake DSM from the combination of diachronic WorldView and Pleiades images (Table S1). On the other hand, we used a 2 m resolution pre-earthquake DSM from Willis *et al.* (2019) that we resampled to a 0.5 m resolution. The DSM from Willis *et al.* (2019) was computed from WorldView and GeoEye images acquired in 2008 and 2016, and processed using COSI-Corr (Leprince *et al.*, 2007). For seven tiles out of 14 (Table S2), we chose to use the DSM from Willis *et al.* (2019), because the charge-coupled device (CCD) artifact from the WorldView sensor was too large in our own DSM and impacted our correlation results (Fig. S2). The external DSM from Willis *et al.* (2019) is oversampled and introduced into the MicMac chain to generate the ortho-images. It is coregistered with the Pleiades data based on the georeferencing information. For the postearthquake dataset, postearthquake DSMs were computed directly from the tri-stereo Pleiades acquisitions (Table S1). Images and DSMs processed with MicMac are automatically coregistered during the processing. Eventually, all images were orthorectified using the MicMac package.

The subpixel correlation was performed between all possible pairs of ortho-images. Because two to three pre-earthquake images as well as three postearthquake images were orthorectified for each tile (Table S2), we obtained between six and nine correlation results for each displacement component (east–west and north–south). Thus, for each component, we calculated a mean displacement map from all the correlation results, with a weighting based on the correlation score map of each correlation result, to average out noise and to obtain the cleanest possible displacement maps.

Finally, we computed the difference between the pre-earthquake and postearthquake DSMs to obtain the vertical displacement field. We used the north–south and east–west displacement maps computed previously to account for the horizontal displacement of the corresponding pixels between the pre-earthquake and postearthquake DSMs. We used a

bivariate spline approximation to sample the postearthquake DSM. Provided that our horizontal displacement maps are correct, this approach ensures that we measure only elevation differences due to the vertical displacement of the earthquake, and that we do not introduce biases due to the topographic mismatch associated with horizontal displacements (Delorme *et al.*, 2020). Vertical uncertainty associated with the DSMs processed with MicMac is close to the ground resolution, which is 0.5 m (Rupnik *et al.*, 2018). Vertical uncertainty for the 2 m pre-earthquake DSMs is not reported in Willis *et al.* (2019). Topographic noise in the vertical displacement maps arises from both vertical errors in the DSMs and, in some areas, an imperfect match between the 0.5 m DSMs processed with MicMac and the oversampled 2 m DSMs from Willis *et al.* (2019).

The 14 tiles of ground displacements in the east–west, north–south, and vertical components were computed independently; thus, they need to be brought together into a common reference frame and be denoised to obtain consistent displacement maps for the whole Ridgecrest rupture. For that purpose, first, the tiles were corrected one by one from spurious signals like linear stripes (CCD artifacts) and sinusoidal artifacts (residual signal from microvibrations of the satellite), by modeling this noise in areas that do not include coseismic signal and then by subtracting the artifacts model from the whole tile. Next, we removed a linear ramp in each tile using neighboring tiles as a reference, assuming that the tiles must overlap in values in common areas. However, in the horizontal components of displacements, this procedure could introduce a long wavelength drift across the full mosaic, as the mosaic is built step by step by aggregation of neighboring tiles. Thus, to ensure that our correction method does not add supplementary artifacts to the final displacement maps, we compared our final horizontal maps to 10 m resolution displacement maps that we computed from correlation of Sentinel-2 optical images (Fig. S3). Only one Sentinel-2 optical scene is needed to cover the entire Ridgecrest area. Because the displacement maps derived from Sentinel-2 include zones with known zero deformation, they can be corrected for any large-scale drift to ensure that these zero-deformation zones are actually equal to zero. These lower-resolution data were then used as a reference to correct potential large-scale trends in our high-resolution results and to ensure that long wavelength signals in our displacement maps represent coseismic deformation and not artifacts. For the vertical component, the coseismic signal is mostly limited to the near-fault domain, so we extracted a linear ramp in each tile to remove any large-scale offset to a zero reference. Then, the tiles were merged.

We checked the low-frequency corrections applied to our displacement maps against GNSS data from Floyd *et al.* (2020). Only three points are located within our study area, which is limited to a width of 4–5 km on each side of the fault. For these three points, the difference between our data and the GNSS data, in the east and north components, ranges from 0.04 to 0.44 m. The mean difference is 0.15 m for the east component and 0.19 m for the north component. However, these comparisons are of limited utility, because they are based only on three points. Also, the time period used to account for the earthquake deformation is much smaller in the GNSS dataset (2–9 July 2019) than in the optical-image dataset (from 2012–2018 to September 2019), leading to supplementary discrepancies between the two datasets.

DESCRIPTION OF THE RESULTS AND COMPARISON WITH INDEPENDENT DATA

Description of the rupture geometry and of the near-fault displacement patterns

East–west, north–south, and vertical displacement maps (Figs. 2 and 3a,b) reveal a complex surface rupture composed of several tens of fault strands of various lengths (<1–20 km). The results are almost in perfect agreement with the ruptures mapped by DuRoss *et al.* (2020) and Ponti *et al.* (2020), based on field observations crosschecked with geodetic data (e.g., optical, light detection and ranging). In a few cases, however, we identified additional subparallel, or longer, fault strands compared with what was mapped in the field. For example, some cross faults striking northeast, located to the north of the mainshock rupture and along the foreshock surface rupture, were not reported in the field maps but are visible in our maps (examples are indicated in Fig. 2a with white arrows.). These additional fault strands have a length of the order of 1–2 km and accommodate up to a few tens of centimeters of displacement. Thus, they need to be taken into account when considering the total displacement budget. The displacement maps also indicate zones where significant diffuse deformation occurred around the different faults, and particularly at bends and in relay zones. This type of deformation is difficult to measure in the field, because it is spread across large distances from the fault (>500 m), and as it is difficult to find specific markers at the surface that allow for measuring this part of the deformation (e.g., Rockwell *et al.*, 2002). In the optical-based displacement maps, diffuse deformation shows up as large-scale displacement gradients and can be measured. In the example of profile B–B′ (Fig. 2b), we observe a diffuse deformation gradient at a stepover located south of the intersection between the foreshock and the mainshock rupture traces. The zone of diffuse deformation extends ∼1 km to the northeast of the mainshock surface rupture (Fig. 2a) and accommodates up to 1 m of displacement (Fig. 2b).

Using the east–west and north–south displacement maps (Figs. 2a and 3a), we derived in 2D the curl (antisymmetric part of the displacement gradient, Fig. 3c) as well as the dilatational and maximum shear components of strain (Fig. 3d,e), to better image the deformation processes associated with the foreshock and mainshock ruptures. The equation for the maximum shear strain is $\gamma = \pm(\lambda_1 - \lambda_2)/2(\lambda_1\lambda_2)^{1/2}$, with λ_1 as the

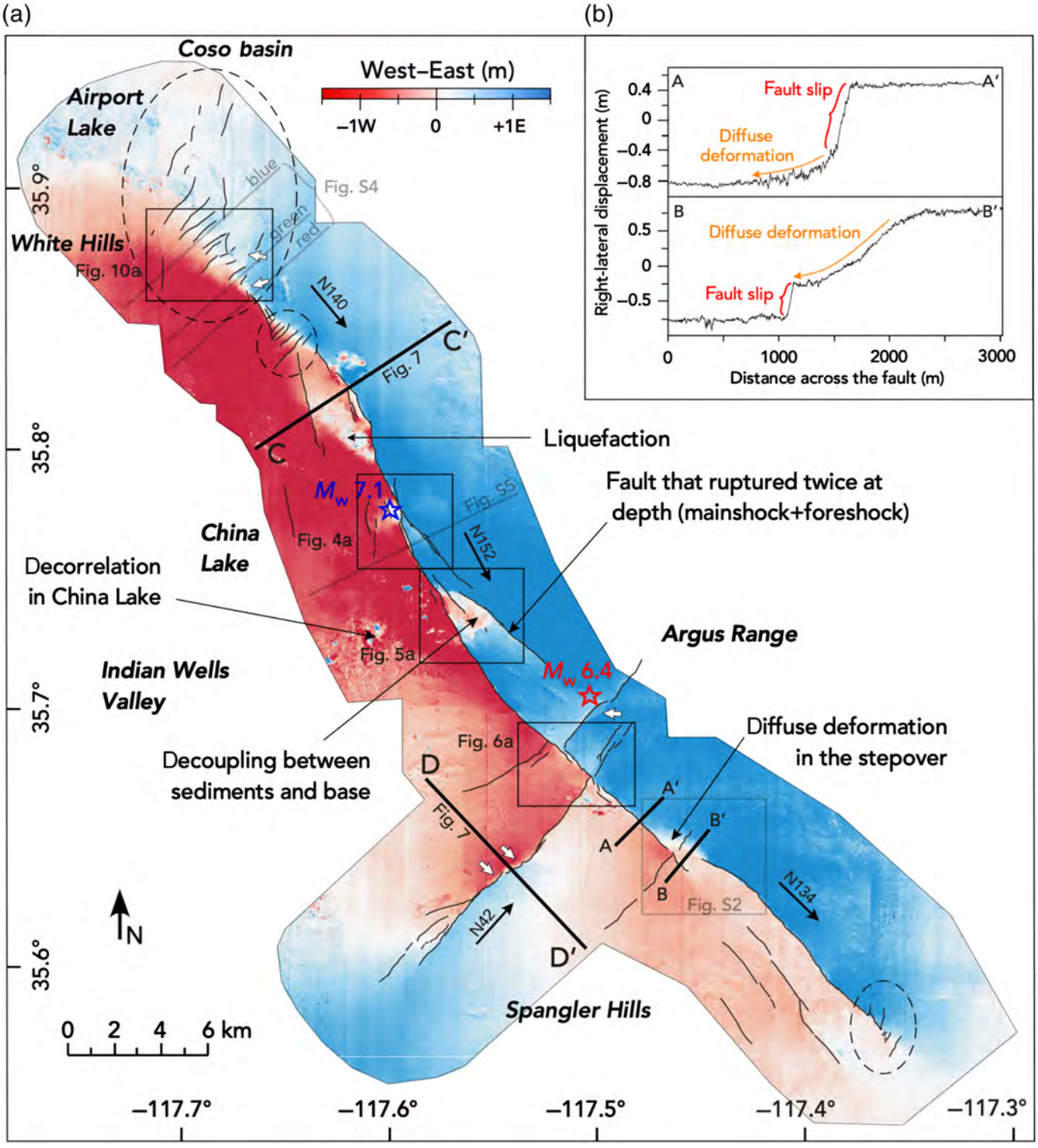

Figure 2. (a) East–west surface displacement map for the 2019 Ridgecrest earthquake sequence. Ground resolution is 0.5 m. USGS epicenter locations (See Data and Resources.) are reported with a red star for the foreshock (35.705° N and −117.505° W) and a blue star for the mainshock (35.77° N and −117.60° W). Surface rupture map from DuRoss *et al.* (2020) is overlaid in black. Examples of fault offsets measured in our displacement maps but not reported in the field are indicated with white arrows. Zones of cross faults striking northeast to the north and south of the mainshock rupture are indicated by dashed circles. Azimuths of the mainshock rupture primary fault trace are indicated at three locations with black arrows. Lateral displacement profiles A–A′ and B–B′, in the fault-parallel component of displacement, are presented in (b). Lateral profiles C–C′ and D–D′ in the three components of displacement are presented in Figure 7. Names of the major topographic features in the region are labeled in bold italic. Location of figures in Appendices is reported in light gray. (b) A–A′ and B–B′ across-fault displacement profiles in the fault-parallel component of displacement. Each swath profile is 100 m wide and 3 km long. Profile A–A′ crosses a linear fault zone, whereas profile B–B′ crosses a relay zone with large diffuse deformation. The color version of this figure is available only in the electronic edition.

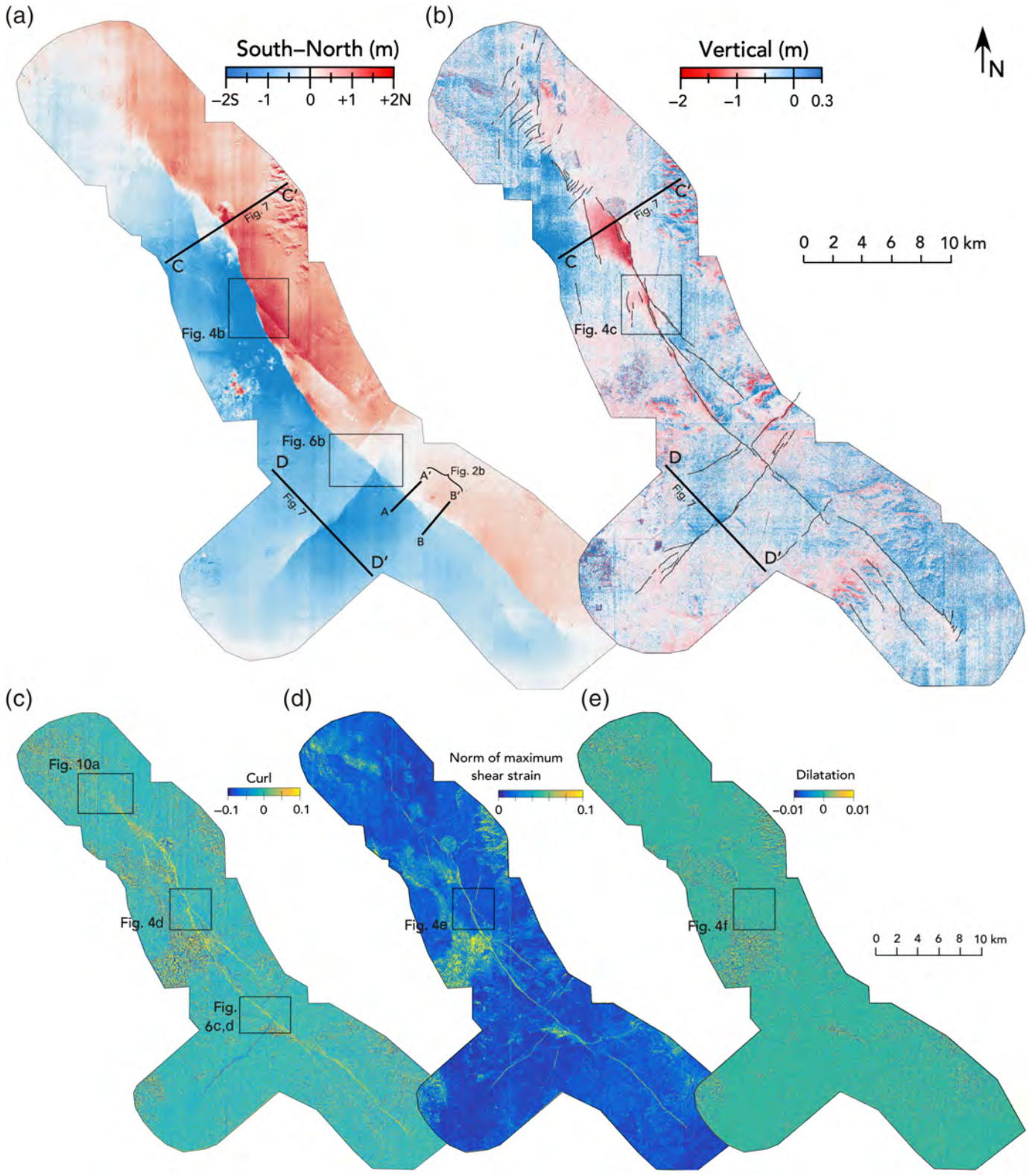

Figure 3. (a,b) Same as in Figure 2a for the north–south and vertical components of displacement. Field rupture map is overlaid in (b). (c) Curl, (d) norm of maximum shear strain, and (e) dilatational strain maps calculated from the horizontal displacement maps at a 5 m ground resolution. Positive curl corresponds to clockwise rotation and positive dilatation to extension. The color version of this figure is available only in the electronic edition.

maximum elongation and λ_2 as the minimum elongation (Ramsay, 1967). The magnitude of this value does not depend on the orientation of the shear. These calculations were performed using MATLAB (see Data and Resources) codes by Allmendinger *et al.* (2012) to calculate the Lagrangian finite strain tensor from horizontal displacement gradients. Before performing the strain calculations, we downsampled the displacement maps to consider only deformation patterns coherent over at least a few meters and to reduce correlation noise (Cheng and Barnhart, 2021). Downsampling the displacement maps is equivalent to applying a low-pass filter, because we consider an "averaged" displacement value over a 2 or 5 m window using the nearest neighbor interpolation. Downsampling was either to a 5 m ground resolution to analyze the rotation and strain patterns at the scale of the whole rupture or to a 2 m ground resolution to analyze details of the rupture in some specific areas.

At the scale of the whole rupture, the curl map (Fig. 3c) reveals a clockwise rotation inside the FZW for the northwest-striking fault sections that ruptured right laterally during the mainshock (faults strike from N133° to N175°, mean azimuth is N140°). An anticlockwise rotation is similarly evidenced inside the surface rupture zone for all the northeast-trending fault sections that ruptured left laterally. The major northeast-trending fault strands, located close to the foreshock epicenter, are associated with the foreshock earthquake, whereas those located around the northern and southern tips of the mainshock rupture are associated with the mainshock earthquake (Ross *et al.*, 2019; Shelly, 2020). The motion evidenced by the curl map (Fig. 3c) is consistent with field-based offsets measurements (DuRoss *et al.*, 2020). The map of the norm of maximum shear strain (Fig. 3d) reveals shear deformation on all the faults identified in the displacement maps (Figs. 2 and 3a,b). A maximum shear strain of 0.1 (10%) is measured along the faults near the center of the rupture, roughly around the mainshock epicentral area. This value is 2 orders of magnitude greater than the maximum possible strain, 0.5%, which can be accommodated by elastic deformation (Lockner, 1998). This 0.5% threshold corresponds to the elastic limit of rocks, calculated as the mean ratio of yield stress to Young's modulus. So, any strain larger than this 0.5% threshold must correspond to inelastic strain. In our case, most of this inelastic deformation actually corresponds to brittle deformation along faults. This 10% value is in agreement with results from Barnhart *et al.* (2020), who also measured surface deformation using image correlation for the Ridgecrest earthquakes. However, unlike Barnhart *et al.* (2020), we do not measure significant dilatational strain across the fault zone (Fig. 3e). Instead, similar to what was found by Milliner *et al.* (2021), our deformation signal is dominated by rotation and shear strain (Fig. 3c,d). This difference in the dilatational strain might be related to the regularization while inverting the surface displacement fields in Barnhart *et al.* (2020). Conversely, our method directly derives 2D strains from the surface displacement fields, without performing any inversion.

To the north of the mainshock rupture, we identify a set of faults that exhibit changes in strike from N42° to N15° when moving northward (Figs. 2a and 3a). These faults form a right-stepping connection with the Coso basin located to the north of the Ridgecrest surface rupture (Jobe *et al.*, 2020). They have a similar orientation to the pre-2019 earthquake structures (Jobe *et al.*, 2020) that relate to the east-northeast–west-southwest (N65°–N75°) extension in the Coso basin (Roquemore, 1980). Just south of this set of faults, near the northern border of China Lake, we observe a 5 km large pull-apart basin bounded by two faults that accommodate slip both in the horizontal and vertical components. This basin is located at a bend in the rupture trace, with the main fault azimuth changing from N140° to N152° in the southward direction. This basin shows evidence of long-term subsidence (Jobe *et al.*, 2020). It also represents the largest subsidence feature along the Ridgecrest rupture, with a maximum vertical displacement of −2 m at its center (Fig. 3b). No ground surface rupture could be identified in the field or in the displacement maps that bound the basin to the south. However, there we measure a sharp gradient of displacement in the east–west and vertical directions (Figs. 2a and 3b), suggesting that a blind fault ruptured at depth. The interior of the basin is characterized by strong decorrelation, which is associated with liquefaction that was recognized in the field by Zimmaro *et al.* (2020).

The M_w 7.1 epicenter is located just south of this pull-apart basin. At least eight distinct fault strands accommodated deformation in this area (Fig. 4a). Altogether, they define an extensional jog with up to 2 m of subsidence (Fig. 4c). Most of these structures were reported in the field map (DuRoss *et al.*, 2020; Ponti *et al.*, 2020), although the detail of the structures and associated diffuse deformation zones could not be resolved using discrete measurements. In this area of the rupture, fault strand 5 is considered to be the primary fault, because it represents the longest continuous fault strand and accommodates the most prominent right-lateral strike slip along the mainshock rupture. In the subsequent discussion, we refer to other faults observed in this region as secondary fault strands.

In the epicentral area, fault strands 5, 10, and 11 accommodate the largest amounts of rotation (Fig. 4d,g) and shear strain (Fig. 4e,h). Fault strands 5 and 10 are subparallel and likely connect at shallow depth. Our results suggest that coseismic displacement is distributed equally between these two strands (Fig. 4h). Similar observation is made for fault strands 5 and 11. Conversely, secondary fault strands 7, 8, 9, 12, and 13 accommodate very little rotation and shear strain, and are barely detectable in the profiles (Fig. 4g,i). When looking in detail at the surface rupture pattern, we can still detect limited areas of contraction or dilatation associated with variations in the rupture azimuth. Fault strands from the extensional jog at the center of this area (faults strands 5, 7, 8, and 9) display

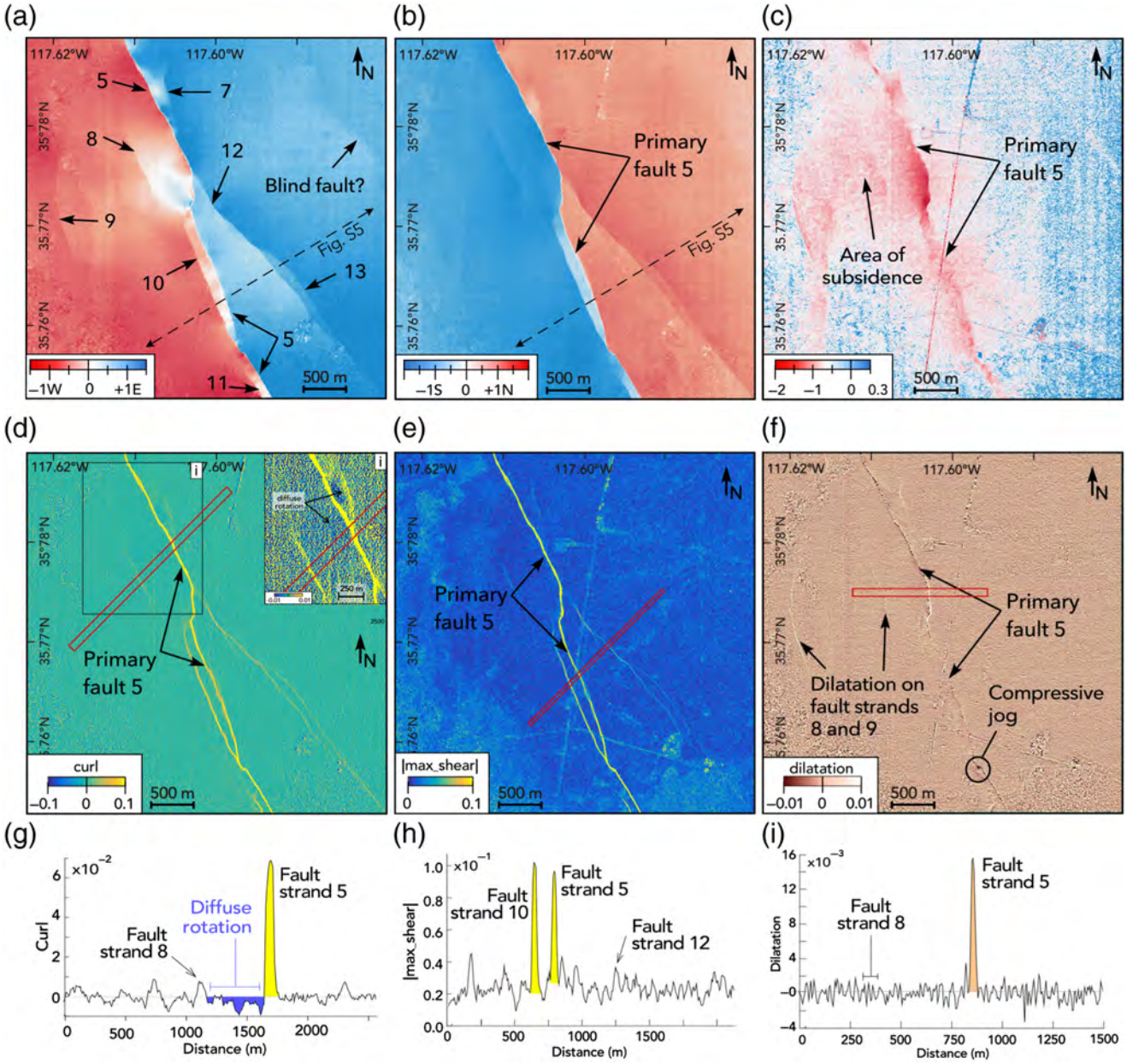

Figure 4. (a–f) Displacement, rotation, and strain maps for the epicentral area of the M_w 7.1 Ridgecrest earthquake. (a) East–west, (b) north–south, and (c) vertical displacement maps. (d) Curl, (e) norm of maximum shear strain, and (f) dilatational strain maps at 5 m ground resolution. Inset in (d) shows an area of diffuse rotation with adjusted color scale. Profiles across the fault zone in the curl, norm of maximum shear strain, and dilatation maps are presented in (g), (h), and (i), respectively. Profiles in (g) and (i) are 50 m wide. Profile in (h) is 25 m wide. High-frequency noise results from ground texture variations. Fault labels as in Figure 9a. The color version of this figure is available only in the electronic edition.

positive dilatation, meaning that some opening occurred on those strands (Fig. 4f). This is also consistent with the subsidence that we measured in the area (Fig. 4c). Compressional strain is conversely measured in the small compressive jog between fault strands 10 and 11 (Fig. 4f). Figure 4f shows, however, that for sections with an azimuth close to N152° (mean azimuth in this area of the rupture), the dilatation pattern is mostly close to zero, alternating frequently from dilation to compression. Milliner *et al.* (2021) suggested that this pattern could be a consequence of variations in the curvature of the fault at length scales of hundreds of meters, which represent small alternate transtensional and transpressional bends. At a much smaller scale, we propose that pixel-by-pixel discrepancies in the east–west and north–south displacement maps in the fault zone can result in such high-frequency variations in the dilatational strain.

In addition to complex localized deformation, the epicentral area is also characterized by some diffuse deformation. One example is the potential blind fault identified to the northeast of the area imaged in Figure 4a. At this location, a fault was neither mapped in the field nor could a localized offset be

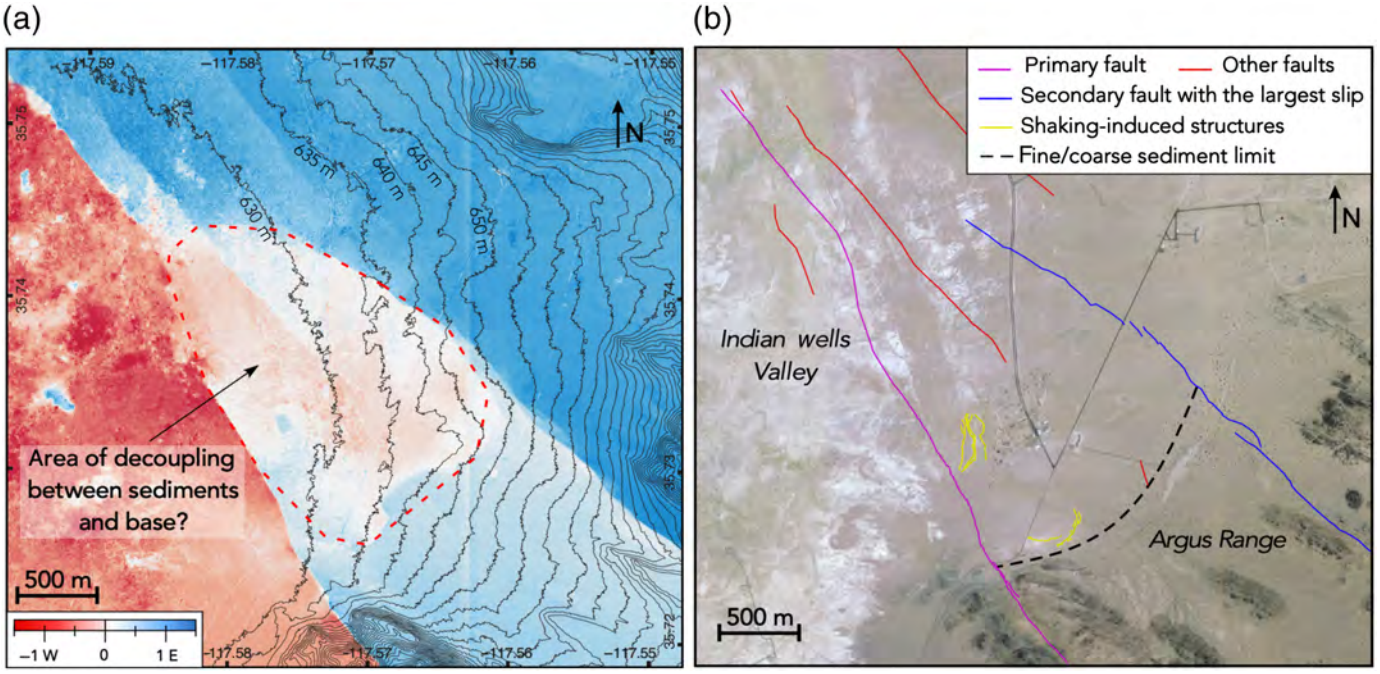

Figure 5. (a) East–west displacement map along the mainshock surface rupture where decoupling between the sediments and the base rocks is observed. Contour lines are extracted from a pre-earthquake digital surface model (DSM) at 2 m ground resolution (Willis *et al.*, 2019). (b) Landsat image of the surface rupture captured on 14 July 2019. Surface rupture map is from DuRoss *et al.* (2020) and shaking-induced structures from Ponti *et al.* (2020). The southeastern limit of the decoupling area seems to correspond to the limit between fine sediments from Indian Wells Valley and coarser deposits from the Argus Range (black dashed line). This limit is inferred from the variation in texture of the deposits visible on the images. The color version of this figure is available only in the electronic edition.

detected in the displacement map. However, we could measure about 0.10 m of right-lateral diffuse deformation across that feature. Diffuse deformation pattern is also visible in the displacement maps between fault strands 5, 7, and 8 (Fig. 4a), and it appears as negative rotation (anticlockwise) in the curl map (Fig. 4d,g). This pattern occurs in response to right-lateral slip on subparallel fault strands 5, 7, and 8.

South of the mainshock epicentral area, a large secondary subparallel fault located east of the primary fault trace (Fig. 5b) corresponds to a right-lateral fault that ruptured twice at depth during the foreshock and the mainshock earthquakes (Ross *et al.*, 2019; Huang *et al.*, 2020; Wang and Bürgmann, 2020). Even if there is no unambiguous evidence that slip reached the surface on this northwest-striking fault during the foreshock (DuRoss *et al.*, 2020; Milliner and Donnellan, 2020), this rupture is located above one of the seismic subevents forming the foreshock (Ross *et al.*, 2019). Between this fault strand and the primary fault strand, we observed a small area that moved west, whereas the rest of the block moved east (Fig. 5a). Optical satellite images at this site show that this area is characterized by very fine sediments, likely clay, with multiple subparallel shorelines associated with successive high stands of the China Lake. These shorelines are outlined by whitish evaporite salt. Deposits of fine clay sediments are visible at the foot of the Argus Range (Fig. 5b). Correlation can be observed between the shape of the displacement pattern on its southeastern extremity and the shape of the contour lines, suggesting some slope-instability process. Thus, we propose that this zone is located in between the two ruptures strands for which motion seems inconsistent with the general deformation pattern and is associated with local decoupling of the upper sedimentary layers from deeper units during lateral spreading of the clay-rich sediments in response to the earthquake shaking. This interpretation is consistent with documentation of shaking-induced structures in the field by Ponti *et al.* (2020).

Farther south, the mainshock rupture deviates to an azimuth of N134° and crosses the foreshock surface rupture (Fig. 2a). At the exact junction between these two ruptures, we cannot identify structures from the foreshock that were offset by the mainshock in the displacement maps (Fig. 6). In fact, we count 11 different northeast-trending fault strands, including the two major left-stepping structures (indicated with larger arrows in Fig. 6a), which stop at the junction with the mainshock; seven northeast-trending faults strands are visible on the southwestern side of the mainshock rupture, and four northeast-trending fault strands are visible on the northeastern side of the mainshock rupture (Fig 6a). However, it appears that none of these fault strands clearly crosses the mainshock fault. Instead, we observe that the two major left-stepping structures stop at the mainshock fault and split into smaller fault strands on the other side. The two major strands of the foreshock rupture that are located, respectively, east and west

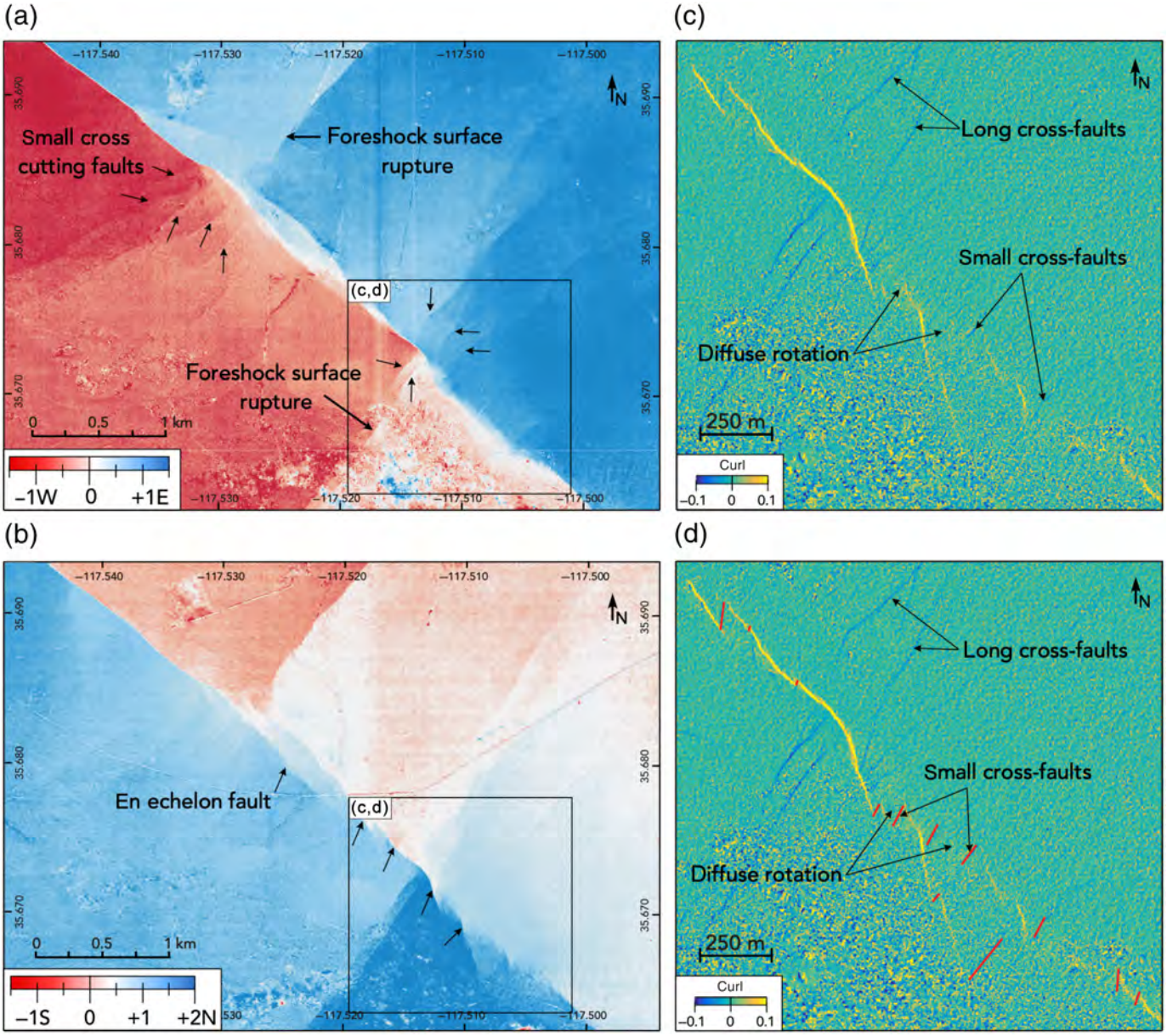

of the mainshock rupture show an apparent left-lateral offset of about 2 km across the main fault zone. This is inconsistent with the right-lateral sense of motion of the mainshock fault and suggests that the foreshock rupture propagated on two distinct structures on either side of the mainshock causative fault. One possible explanation is that the fault that was activated during the mainshock is likely more active and accumulates larger deformation at the fault zone than the one activated during the foreshock, because the main fault is more closely aligned with the current regional deformation pattern. Thus, the main active fault zone may represent a barrier for the propagation of the foreshock rupture.

In this area, the displacement associated with the mainshock rupture is, at a first order, accommodated by one primary fault (Fig. 6). However, when zooming on the junction, we can see that this primary fault is in fact formed by a series of

Figure 6. (a) East–west and (b) north–south displacement maps at the junction between the foreshock and mainshock surface ruptures. Small cross faults indicated in (a) are examples of very small faults (roughly aligned with the foreshock azimuth) that were for the most part not mapped in the field (Fig. 2a). In (b), en echelon faults in the trace of the mainshock surface rupture are indicated by black arrows. Only the major one, labeled "en echelon," was mapped in the field (Fig. 2a). (c) Map of the curl at 2 m ground resolution for a zoom area in (a) and (b) (See location in a,b.). Long cross faults belong to the foreshock surface rupture. Small cross faults located between the en echelon faults belong to the mainshock surface rupture. Diffuse rotation is visible between the small cross faults, indicated by denser yellowish color between faults. (d) Interpreted curl map with the visible cross faults belonging to the mainshock rupture mapped in red (0.1–0.4 m of north–south [N-S] slip). The color version of this figure is available only in the electronic edition.

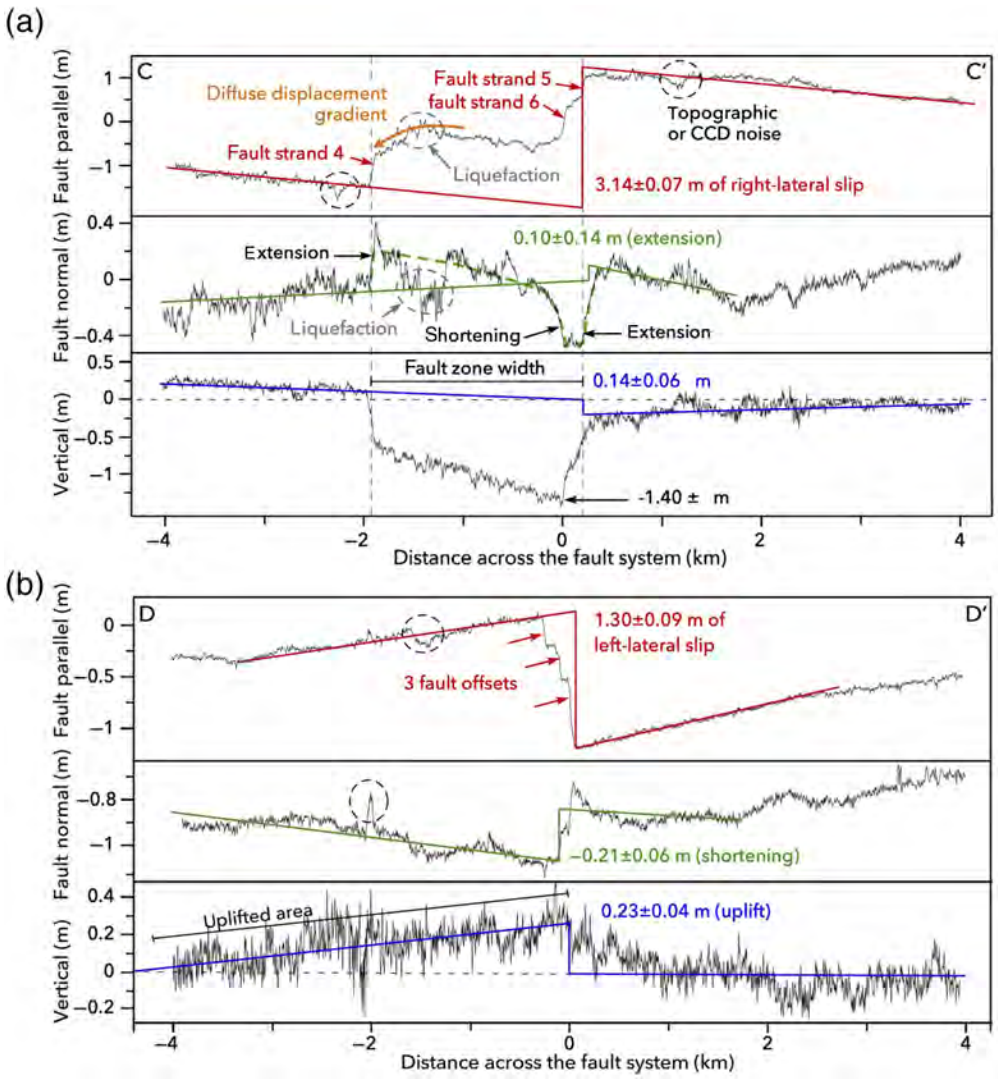

Figure 7. (a) Fault-parallel, fault-normal, and vertical displacements along profile C–C′ (Fig. 2a) across the pull-apart basin in the mainshock surface rupture. Faults 4 and 5 are antithetic and dip toward the center of the basin with an angle of 40° (fault-dip angle is the arctan of vertical displacement over fault-normal displacement). (b) Fault-parallel, fault-normal, and vertical displacements along profile D–D′ across a compressional jog along the foreshock surface rupture (Fig. 2a). For each profile, the linear regression used to measure the displacement is shown by colored lines. Error associated with the offset values corresponds to std2. A zone of diffuse deformation along C–C′ is indicated with an orange arrow. Interpreted fault-normal C–C′ profile is proposed (dashed green) in the fault zone. Noise circled in gray in C–C′ corresponds to liquefaction identified in Zimmaro *et al.* (2020). Other types of noise, generally associated with charge-coupled device (CCD) camera and orthorectification issues, are indicated at few locations with black dashed circles. The color version of this figure is available only in the electronic edition.

en echelon, left-stepping faults oriented in the north–south direction (Fig 6b). These en echelon faults are connected by subparallel sinistral faults (Fig. 6c,d). These sinistral faults have similar orientations to the faults associated with the foreshock. Diffuse clockwise rotation is also evident between those faults (Fig. 6d).

South of the junction with the foreshock rupture, the mainshock surface displacement is accommodated by two primary faults separated by a stepover (Fig. 2a). Several secondary faults located southwest of these primary faults are visible in the field rupture map (Fig. 2a) and slipped ~0.20 m. The mainshock surface rupture terminates to the southeast into a set of several small left-lateral faults with azimuths such as those of the foreshock, the faults mapped to the northern end of the rupture (Fig. 2a), and at the junction between the mainshock and the foreshock (Fig. 6). All these structures accommodate left-lateral horizontal motion (Fig. 3c).

Quantification of fault-parallel, fault-normal, and vertical displacements along the ruptures

In the following section, we document along-strike variations of the horizontal displacements, decomposed into fault-parallel and fault-normal directions, as well as of the vertical component, and we analyze the results with respect to the fault geometry described previously.

Swath profiles 100 m wide and 8 km long placed perpendicular to the local strike of the rupture are used to characterize the processes accommodating deformation in the fault zone. Here, we focus on quantifying the number of fault strands activated with their respective amount of slip, and the diffuse deformation for the foreshock (Fig. 7a) and mainshock surface ruptures (Fig. 7b). The criteria used to differentiate localized fault slip from diffuse deformation are the angle and the shape of the displacement gradients. Localized fault slip shows up in profiles as subvertical linear gradients with well-defined extremities. Conversely, diffuse deformation shows up as long-wavelength gradients with smooth transitions toward the far-field trends. Width of the deformation zone cannot be used as a criterion to differentiate localized slip on a surface fault strand and diffuse deformation in the bulk medium. In fact, large-amplitude localized fault slip can generate a deformation

zone several hundred meters wide (Faulkner *et al.*, 2011; Fig. S4). Conversely, a rupture zone with a low-amplitude total offset accommodated through diffuse deformation can occur over a limited width of a hundred meters (e.g., blind fault in Fig. 4a). Diffuse deformation is essentially described in the fault-parallel component of displacement, because fault-normal and vertical displacement profiles are more affected by noise; thus, the difference between diffuse gradients and slip offsets can be ambiguous.

Profile C–C′ (Fig. 7a) goes across the pull-apart basin to the north of the mainshock rupture (Fig. 2a) and shows that the fault-parallel displacement localizes on three different fault strands. Two of these fault strands (fault strands 5 and 6, Fig. 7a) are only 200 m apart and constitute the eastern border of the basin. They likely join at shallow depth. The third fault strand corresponds to the western border of the basin (fault strand 4, Fig. 7a). Fault strands 4, 5, and 6 have ∼40° dip (Fault-dip angle is computed as the arctan of vertical displacement over fault-normal displacement.), although strand 4 dips in the opposite direction of strands 5 and 6, because they correspond to different edges of the basin. Fault strand 5 is the primary fault strand of the rupture, as it continues southward toward the epicenter, whereas the two other strands remain limited to the basin. In this area of the rupture, secondary fault strands 4 and 6 take up to 50% of the surface displacement. Diffuse deformation is also measured inside the basin area. This gradient is in the same direction as the slip offsets (decreasing toward the east), meaning that this zone accommodates right-lateral shear and contributes to the overall budget of displacement across the fault zone. Some decorrelation is visible in this area in the displacement maps (Figs. 2a and 3a) that is related to liquefaction (Zimmaro *et al.*, 2020).

Extension on the C–C′ profile occurs on both sides of the basin with 0.57 m on the western side (fault strand 5, Fig. 7a) and 0.30 m on the eastern side (fault strand 4, Fig. 7a). However, we measure shortening on the fault strand central to the basin (fault strand 6) as well as some diffuse shortening inside of the basin. Similarly, Milliner *et al.* (2021) measured dilatation on fault strands 4 and 5, and contraction on fault strand 6. Our strain calculations (Fig. 3d,e) are consistent with these observations. The maximum subsidence inside the basin along the C–C′ profile (Fig. 7a) is 1.4 m, although the total effective vertical displacement across the basin is only 0.14 ±0.06 m. Total extension across the 2.2 km wide fault zone is only about 0.10 m, which is smaller than the 0.14 m uncertainty on the measurement itself.

Profile D–D′ (Fig. 7b), which goes across a small compressive bend that is located along the foreshock rupture, shows deformation localized on three fault strands for the fault-parallel component. These fault strands are separated from each other only by ∼120 m, and no significant diffuse deformation is accommodated between the localized ruptures. However, shortening and vertical displacements occur only on the two fault strands located to the south, whereas the northern strand accommodates only strike-slip motion. This suggests that some partitioning occurred between the fault-parallel and fault-normal displacements throughout the fault system.

To quantify along-strike variations of surface displacements, we extracted 123 and 460 swath profiles across the surface ruptures associated with the M_w 6.4 foreshock and the M_w 7.1 mainshock, respectively. Swath profiles are similar to those from Figure 7: 100 m wide and 8 km long (Fig. 7), perpendicular to the local strike of the rupture (Fig. 2). Successive profiles are spaced every 120–150 m. For each profile, the total surface displacement was estimated by measuring the offset at the fault location between linear regressions fitting, respectively, the displacements on either side of the fault zone (Fig. 7 and Fig. S5). The parameters of each regression were tuned to fit the greatest arctangent-shape or linear-shape gradients and accommodate the variable width of the fault zone that ranges from highly localized (30–40 m) to widely distributed (∼2.5 km). In addition, each profile was manually inspected and adjusted to make sure that each fit is not biased by spurious data related to noise in the correlation maps. The total displacement measured on the profile includes either localized slip on faults or diffuse deformation, or both, as shown in profile C–C′ (Fig. 7a). Using this method for each profile, we measure the maximum surface displacement. Theoretical precision of the measurement is 0.05 m, but here we consider a conservative uncertainty of 0.10 m to account for the noise that is present in the displacement maps (orthorectification bias and correlation noise). Mean standard deviation for individual offset measurement, referred to as std1, is almost constant along the slip curve. This corresponds to the aleatoric uncertainty arising from the noise in the data. Respectively, for the parallel, normal, and vertical component of displacement, std1 is 0.06, 0.06, and 0.08 m for the mainshock, and 0.09, 0.06, and 0.14 m for the foreshock slip curves. Impact of the positioning of the linear regressions on each side of the fault, which corresponds to the epistemic source of error (std2), was assessed by analyzing independently several times the displacement profiles. These profiles were systematically taken across displacement maps at different resolutions (2, 3, 4, and 5 m, Fig. S5). This allows us to assess the influence of the map downsampling on the measured offsets. We then took the standard deviation over the four displacement values measured at various map resolutions at each point along the ruptures (Fig. S4). Std2 represents the reproducibility and reliability of the measure, and was plotted as an error bar in Figure 8. We separately estimated the mean std2 for the foreshock and the mainshock ruptures, because the amplitude of the displacement and number of profiles are different. In the case of the mainshock, we estimate a mean std2 of 0.07, 0.14, and 0.06 m, respectively, in the fault-parallel, fault-normal, and vertical components. In the case of the foreshock, we estimate a mean std2 of 0.09, 0.06, and 0.04 m, respectively, in the fault-parallel, fault-normal, and vertical components.

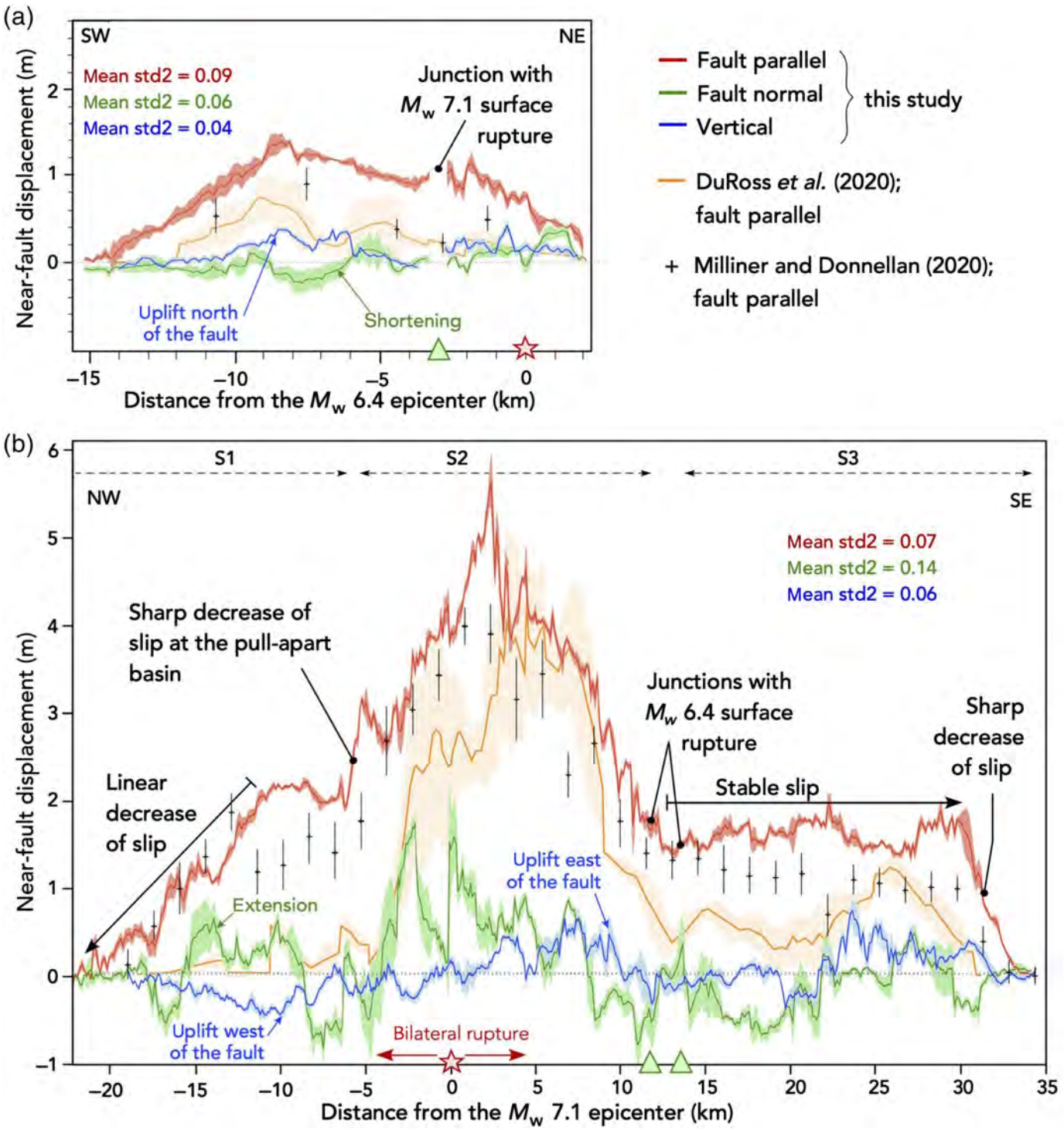

Figure 8. Fault-parallel (red), fault-normal (green), and vertical (blue) slip distributions for the M_w 6.4 foreshock earthquake in (a) and for the M_w 7.1 mainshock earthquake in (b). Epicenter locations (red stars) and junctions between the foreshock and mainshock rupture (green triangles) are projected on the *x* axis. Positive fault-normal displacement corresponds to extension. Positive vertical displacement corresponds to uplift on the northern wall of the rupture for the foreshock and to uplift on the eastern wall of the rupture for the mainshock. Cumulative moving mean of field data from DuRoss *et al.* (2020) are in orange. Optical results from Milliner and Donnellan (2020) in black, cumulated for the mainshock over three of the subparallel fault strands considered in their study. Both datasets (DuRoss *et al.*, 2020; Milliner and Donnellan, 2020) are in the fault-parallel component of displacement. S1, S2, and S3 correspond to the rupture segments discussed in the Localized Slip versus Diffuse Deformation for the M_w 7.1 Mainshock Earthquake section. The color version of this figure is available only in the electronic edition.

We also calculated the coefficient of variation (CV) on our measurements. CV corresponds to the ratio between std2 and the mean value of the displacements, measured in the maps at various resolutions. The mean CV in the fault-parallel component is 0.13 for the foreshock rupture and 0.04 for the mainshock rupture. This highlights that large-magnitude displacements as for the mainshock rupture are less impacted by correlation noise and present a lower variability than lower-magnitude displacements, as observed for the foreshock, which displays a larger CV. In the fault-normal component of displacement, CV is 5.09 and 1.46, respectively, for the foreshock and mainshock ruptures. Because CV is the ratio between std2 and the mean offset value at a point, it tends toward large values when the offset values are close to zero. Hence, the mean CV for the fault-normal component of displacement is likely to be less meaningful because of the recurrent changes from positive to negative sign in the displacements (Fig. 8). Furthermore, CV for the vertical displacement offsets could not be assessed, because a large number of measurements are close to zero, which renders CV essentially infinite.

Fault-zone displacements were easier to estimate in the fault-parallel component, because the signal-to-noise ratio as well as the CV are significantly better. Also, offsets in this component show consistency along strike, either right lateral or left lateral depending on the earthquake (mainshock or foreshock). In contrast, fault-normal and vertical displacements are more variable, following local variations in the fault geometry that result in an additional dip-slip component. Offset measurements for each of the 123 and 460 swath profiles, respectively, taken across the foreshock and mainshock ruptures are projected along the mean rupture azimuth for each earthquake (N42° for the foreshock and N140° for the mainshock). The resulting curves are presented in Figure 8 with the error envelope corresponding to std2 at each profile.

The fault-parallel slip curve for the foreshock earthquake (Fig. 8a) has a concave shape with a peak of maximum left-lateral slip of 1.3 ± 0.09 m at −8.5 km, approximately in the middle of the fault section southwest of the junction with the M_w 7.1 rupture, and a mean left-lateral slip of 0.73 ± 0.09 m. At the southwestern end of the rupture, slip decreases linearly until it reaches zero. Unfortunately, the last kilometer of northeastern termination of the foreshock rupture is not covered by our images. Field- and satellite-based measurements in this area, however, suggest that slip continues decreasing linearly in this direction (DuRoss *et al.*, 2020; Milliner and Donnellan, 2020). We also measure a maximum of 0.2 m of shortening and 0.4 m of uplift between −6 and −8 km, corresponding to the location of a small restraining bend (Fig. 2a), highlighted by profile D–D′ (Fig. 7). The fault-parallel surface-slip distribution for the mainshock earthquake (Fig. 8b) is more complex than for the foreshock earthquake (Fig. 8a). The mean right-lateral slip is 2.13 ± 0.06 m, with a maximum of 5.6 ± 0.06 m located 2.5 km southeast from the epicenter. This maximum peak corresponds to the sum of slip offsets on fault strands 5, 11, 12, and 13 (Fig. 4a), in addition to some diffuse deformation occurring in the surrounding areas. Details of the slip offsets on each fault strand of the rupture are presented in the Localized Slip versus Diffuse Deformation for the M_w 7.1 Mainshock Earthquake section. The variability in the slip function combined with surface rupture azimuth changes suggest that the mainshock rupture is divided into three domains: a maximum slip domain that surrounds the epicenter (S2, −6 to 12 km), a linearly decreasing slip domain northwest of the epicenter (S1, −22 to −6 km), and a constant slip domain where slip is about 1.5 m for 22 km to the end of the rupture (S3, 12–34 km). This last domain is separated from the maximum slip domain by the intersection with the foreshock surface rupture, and it ends abruptly to the southeast where the rupture ends. The length of these three displacement domains S1, S2, and S3, defined based on the surface displacement pattern (Fig. 8b) and the rupture geometry (Fig. 2a), is consistent with rupture segmentation generally observed for continental strike-slip fault ruptures (~18 km, Klinger, 2010); thus, each domain will be referred to as a segment of the rupture.

Deciphering a systematic displacement pattern for the perpendicular and the vertical components of the displacement is more difficult, because each component's amplitude varies substantially along strike. Fault-normal slip curve varies accordingly to the changes in rupture geometry (Fig. 8b). Indeed, extension is measured around the epicentral area and along the whole central section of the rupture (from −5 to 8 km, Fig. 8b), where the fault trend is N152°, 12° clockwise from the N140° mean strike (Fig. 2a). This extension coincides with subsidence in the area (Fig. 4c) and with dilatational strain on several faults (Fig. 4f). Conversely, we measure shortening in an area where the fault deviates by 6° anticlockwise (N134°) from the mean azimuth (8–22 km in Fig. 8b and geometry of the fault in Fig. 2a). As for the vertical component, although it is affected by significant noise, the general trend shows relative subsidence to the east of the rupture along the northwestern section (~−0.50 m) and east-side uplift along the southeastern extent of the rupture (~+0.50 m). A similar long-wavelength pattern has also been observed from radar interferometry (Fielding *et al.*, 2020; Fialko and Jin, 2021). This pattern is coherent with the locations of the compressional and tensional lobes that result from the elastic deformation field of the right-lateral mainshock rupture. Based on the modeling of a dislocation intersecting the free surface in an elastic half-space, Fialko *et al.* (2001) have shown that the vertical uplift at the tips of the 1999 Hector Mine strike-slip rupture represents 10% of the strike-slip offset. These findings agree well with the ratio of about 0.50 m of vertical motion for about 5 m of horizontal displacements measured in our study (Fig. 8b). At a larger scale, the coseismic vertical displacement (Fig. 3b) is consistent with the long-term landscape morphology; the area of the current depocenter of

China Lake as well as the basin located to the northeast of the rupture (close to the Coso area) have subsided during the earthquakes. In contrast, the area northwest of the northern rupture termination is uplifting, which is consistent with the presence of the White Hills mountain anticline (DuRoss *et al.*, 2020; Jobe *et al.*, 2020).

A comparison of our results in the fault-parallel component with optical results from Milliner and Donnellan (2020) and field data from DuRoss *et al.* (2020) reveals that our measurements are generally larger than prior work. This result also applies to previously published higher resolution optical image-based studies (Gold *et al.*, 2021; Milliner *et al.*, 2021; Fig. S6). A first explanation regarding results from Milliner and Donnellan (2020) is that they use lower-resolution images combined with large correlation windows (Input image resolution is 3–5 m, and output resolution of the displacement maps is 87 m.), which might result in averaging out the displacement signal over large areas, leading to an underestimation of the peak signal. A second explanation regarding all optical-based results relates to the method used to measure the total displacement. In this study, we include diffuse deformation gradients taken over a wide aperture (>500 m) that might arise from variations of slip on the fault plane at shallow depth. As described previously in this study, diffuse deformation might include the elastic response of the medium to subsurface slip, in addition to surface inelastic deformation. Thus, our data represent the maximum displacement envelop for this rupture. It includes all the measurable surface displacements in the rupture area, up to a few kilometers away from the primary fault, without distinction on the type of deformation. Other studies do not incorporate these large-scale gradients into their surface-slip estimations. They focus on fault displacement and local OFD over apertures of a few hundred meters (Milliner and Donnellan, 2020; Gold *et al.*, 2021; Milliner *et al.*, 2021), and provide estimations of the surface inelastic deformation along major faults. Finally, regarding the field observation, as already observed for previous events (Klinger *et al.*, 2005; Milliner *et al.*, 2015; Zinke *et al.*, 2019), the field data usually only include offsets along localized deformation structures. In fact, except in unusual cases in which long piercing lines are available (Rockwell *et al.*, 2002; Rockwell and Klinger, 2013), it is difficult to incorporate diffuse deformation into field measurements. Thus, the field data generally report a minimum measurement of fault displacements compared with a more integrated measurement performed by image correlation (Delorme *et al.*, 2020).

Localized slip versus diffuse deformation for the M_w 7.1 mainshock earthquake

Although in the previous sections we had systematically integrated the deformation across the entire rupture zone (Fig. 8b), in the following we examine the detail of the individual slip distribution for 20 fault strands along the mainshock rupture that can be recognized in our horizontal displacement maps (Fig. 9a,b). Hence, in many places, this involves looking at the individual slip distribution for several subparallel rupture strands. Still, faults shorter than 1 km were aggregated with the largest structure nearby. Also, individual faults have widths ranging from a few meters to a few hundred meters (e.g., red profile in Fig. S4) and include some of the rock damage that occurs in the direct vicinity of the fault structure. This is different from what is generally done in other studies that estimate localized deformation on visible fractures of widths of a few meters only and fault damage over scales of a few hundred of meters (Cheng and Barnhart, 2021; Gold *et al.*, 2021). Hence, by subtracting the sum of the localized deformation along each different rupture strand from the deformation integrated over the whole fault zone (Fig. 8b), we estimate the amount of diffuse deformation, corresponding to the long-wavelength and low-amplitude gradients of deformation that occurs away from the primarily visible deformation areas (e.g., Fig. 2b, profile B–B′) at every location along the rupture (Fig. 9b).

Faults in gray in Figure 9a did not accommodate right-lateral slip and were not included in the fault displacement budget. They accommodated either left-lateral slip (for the northeast-trending faults) or extensional deformation (faults west of the epicenter). Also, any individual structure accommodating 0.10 m or less of right-lateral slip is likely below our detection threshold and considered as part of the diffuse deformation contribution to the total displacement budget. For all individual fault strands, Figure 9b shows that our measurements are in good agreement with the data collected in the field. As discussed earlier, our measurements usually correspond to the maximum envelop of the field data. Part of the reason for that might be short or low-quality piercing lines, which make the documentation of diffuse deformation in the field difficult, if not impossible (McGill and Rubin, 1999). A couple of field datapoints appear to be larger than what we could measure in the correlation map. These points, however, have large uncertainties, and our measurements agree within error. Thus, the overall consistency between our dataset and the field measurements validates our measurement methodology based on the swath profile analysis and strengthens our assessment of the diffuse component of the total displacement budget.

The distribution of the diffuse deformation along strike follows a pattern similar to that highlighted by the distribution of the total fault-parallel slip (Fig. 8b) and the rupture geometry (Fig. 9a). Along the first segment (S1), diffuse deformation (gray domain, Fig. 9b) dominates the total displacement budget (black curve, Fig. 9b), whereas localized deformation remains limited along fault strands 1, 2, and 3 (colored curves, Fig. 9b). When moving toward the epicenter, the amount of diffuse deformation increases in parallel with the total displacement budget. At its maximum along segment S1, diffuse deformation reaches 2 m in places where no localized deformation in the right-lateral direction is observed at the ground surface. Along fault strand 3, where localized deformation is

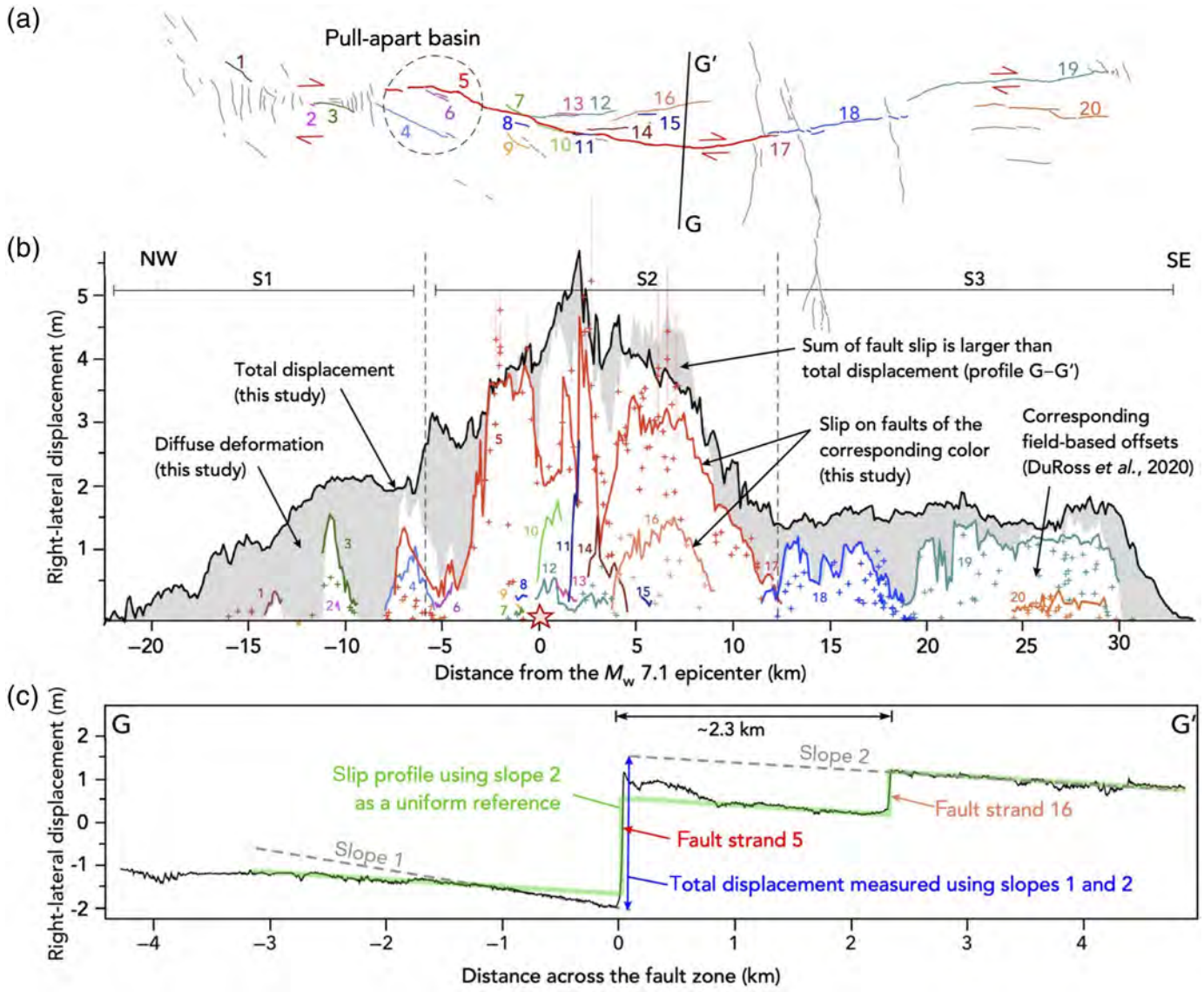

found, the diffuse deformation represents 25% of the total displacement budget for the fault-parallel component. In total, diffuse deformation in this region of the rupture represents 81% for a mean right-lateral slip of 1.21 m.

Segment S2 is separated from S1 by the large pull-apart basin. There we measured an abrupt increase of slip on fault strand 5 from −4 to −3 km (~0.5–3.5 m, Fig. 9b). Along segment S2, beside the pull-apart area that bounds the segment to the north, most of the deformation is localized on the fault strands up to 100% of the total deformation in several places. Only 18% of the surface displacement budget is accommodated through diffuse deformation in S2 for a mean right-lateral slip of 3.53 m. The fault pattern described based on field observations (DuRoss *et al.*, 2020) is complex with the slip distributed on several subparallel fault strands. Fault strand 5 is the primary fault strand that in many places accommodates more than 60% of the total localized slip. In addition to fault strand 5 at the center of the rupture, 11 secondary fault strands accommodate displacement. The secondary fault strands

Figure 9. (a) Map of the 2019 Ridgecrest mainshock surface rupture from DuRoss *et al.* (2020). Colors and corresponding labels indicate the 20 continuous fault strands for which we have collected individual slip profiles. (b) Total displacement (black, from Fig. 8b) versus localized fault slip (colored lines). Field datapoints for each fault strand are shown indicated by similarly colored crosses. For sake of clarity, error bars for field data are shown only for data above our total displacement budget. The sum of the localized slip is shown in white and the diffuse deformation (total displacement minus localized slip) in gray. (c) G–G′ fault-parallel displacement profile taken across the area where an excess of fault slip is measured relative to the total displacement budget in (b). Dashed gray lines correspond to the linear regressions (slopes 1 and 2) used to measure the total surface displacement in blue. Green profile represents a possible slip profile using uniform slip gradients inside the fault zone (slope 2). A component of apparent left-lateral shearing near fault strand 5 leads to an excess or overshoot of fault slip over total displacement. The color version of this figure is available only in the electronic edition.

accommodate up to 40% of the total displacement budget in some locations along S2. Fault strand 16 constitutes the largest of these secondary faults and accommodates up to 1.5 m of slip (profile G–G′, Fig. 9c). Secondary strands 7, 8, 9, 10, 11, 13, and 15 are shorter (~1 km) but can individually accommodate amounts of slip comparable to fault strand 16.

In the area where fault strands 5 and 16 run parallel to each other (4–8 km, Fig. 9b), a comparison of the total displacement including diffuse deformation for the whole width of the fault with the cumulative slip offsets measured on each strand of the fault zone indicates that there is an excess of slip in the near field relative to the total displacement budget (Fig. 9b). This apparent excess of slip is not included within the 18% of diffuse deformation we calculated along S2. In this particular area, the displacement profiles are strongly asymmetric (slopes 1 and 2, Fig. 9c), and slip gradients in the first kilometer around fault strand 5 are much higher than around fault strand 16. This implies an excess of surface slip on fault strand 5 within the first kilometers of the crust compared with what one would expect when projecting the gradients around fault strand 16 (green profile, Fig. 9c). This local increase in horizontal slip is also visible on the displacement maps from Barnhart *et al.* (2020). We could not rule out the effect of the prominent bedrock ridge east of fault strand 5 on the orthorectification process due to potential inaccurate topographic determination during the DSM calculation. Our measurements of the vertical motion in this area through the DSM differencing, however, are consistent with field observations (30–50 cm; DuRoss *et al.*, 2020), making the case of spurious topography unlikely. The fact that this excess slip is located along the section of fault that ruptured during the foreshock earthquake may not be a coincidence. We could hypothesize that the right-lateral prerupture of fault strand 16 at depth during the foreshock earthquake (Ross *et al.*, 2019; Huang *et al.*, 2020; Wang and Bürgmann, 2020) locally increased stress within the upper few kilometers of fault strand 5, making fault strand 5 more prone to slip during the mainshock rupture. Unfortunately, current models of Coulomb stress variations based on slip inversion do not have the spatial resolution to further address this issue.

Segment S3 corresponds to an area where the slip distribution for the fault-parallel component remains almost constant, around 1.5 m, for a distance of 22 km from the junction with the foreshock rupture to the southern tip of the mainshock rupture. In this area, displacement is primarily localized on fault strands 18 and 19 that accommodate slip up to a maximum of 1 and 1.3 m, respectively. These two faults are connected by a 1 km long relay zone where up to 1 m of fault-parallel shear is accommodated through diffuse deformation (profile B–B′ in Figs. 2b and 9b). There, the proportion of diffuse deformation approaches 80%. Conversely, toward the southern end of the rupture where fault strands 19 and 20 are parallel, the amount of diffuse deformation is close to zero. Fault strand 20 is subparallel to fault strand 19, and it accommodates only a small amount of slip (~0.20 m). Additional faults were mapped by Ponti *et al.* (2020) in this area, but they do not correspond to visible slip offsets in our surface displacement maps. Diffuse deformation in S3 represents 39% of the total surface displacement budget for a mean right-lateral slip of 1.42 m. For the entire length of the mainshock rupture, diffuse deformation represents 31% of the surface displacement budget. Similar amounts of diffuse deformation were also inferred along the foreshock rupture where 31% of the total left-lateral displacement is accommodated through diffuse deformation (Figs. S7 and S8).

DISCUSSION

Two sets of orthogonal faults and their impacts on the surface displacements

Although the main rupture follows a general trend oriented northwest, the Ridgecrest earthquakes displacement field is also characterized by the activation of a second set of cross faults trending N42°, perpendicular to the mainshock surface rupture, including the ground ruptures associated with the foreshock. In addition to the foreshock rupture already documented in previous studies (e.g., Barnhart *et al.*, 2020; Chen *et al.*, 2020; DuRoss *et al.*, 2020; Milliner and Donnellan, 2020), a large number of secondary faults associated with the mainshock rupture also align along the N42° trend. One several kilometer long fault located south of the foreshock rupture, well mapped in the field (DuRoss *et al.*, 2020), crosses the mainshock ruptures between fault strands 18 and 19 (Fig. 9a), and can be followed for several kilometers. This oblique-slip cross fault accommodates 0.15 m of left-lateral slip and 0.15 m of shortening in the area south of the connection with the mainshock rupture. We identified smaller scale northeast-trending faults in the relay zone between faults 18 and 19 (Fig. S2b) alongside this long northeast-trending cross fault. We also mapped smaller northeast-trending faults at the junction between the foreshock and the mainshock ruptures (Fig. 6). Finally, the northern and southern tips of the mainshock rupture are characterized by faults with similar azimuth (Figs. 2a and 10). Many of these faults, with the exception of those observed at the junction between the foreshock and mainshock ruptures (Fig. 6), were identified in the field (DuRoss *et al.*, 2020). Their displacement, however, could generally not be quantified in the field due to the lack of unambiguous markers.

At the northern end of the mainshock rupture, the zone of northeast-trending cross faulting occurs over a 10 km distance in the northwest direction (Figs. 2 and 3a) and is located at the transition with the Coso basin (Fig. 2a). Only a few of these faults could be identified as predating the 2019 rupture (Jobe *et al.*, 2020). In this zone, the displacement maps reveal that the right-lateral deformation associated with the mainshock is the dominate style of deformation (Figs. 2a and 3a). However, with the exception of a short section, where dextral deformation is localized at the ground surface between two zones of northeast-trending faults (fault 3, Fig. 9a), the localized dextral

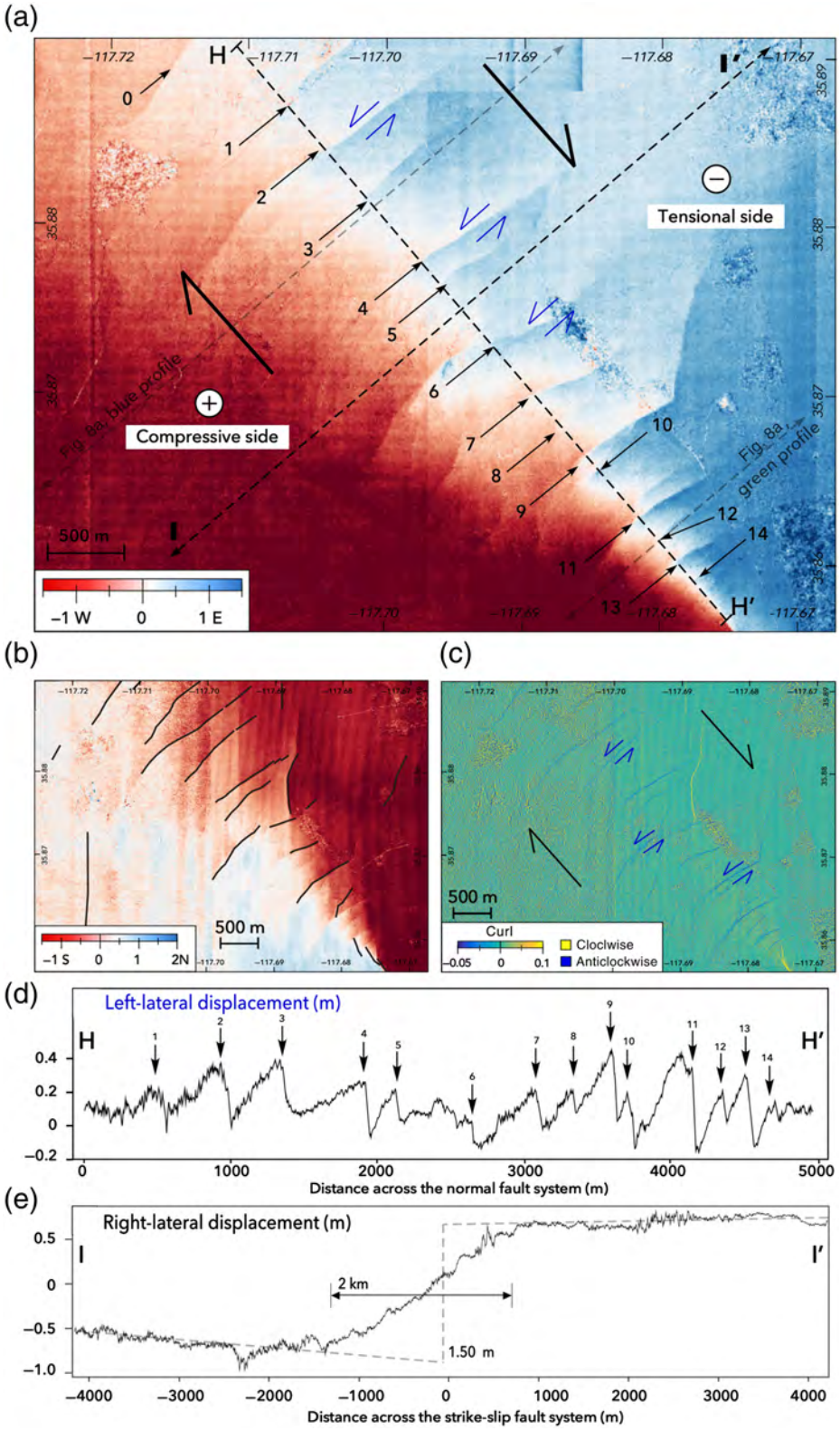

Figure 10. (a) East–west and (b) north–south displacement maps to the north of the mainshock rupture, where northeast-trending faults ruptured the surface (see Fig. 2a for location). Rupture map from DuRoss *et al.* (2020) is overlaid in black in (b). (c) Curl map calculated from horizontal displacement maps downsampled at 2 m. Blue corresponds to anticlockwise rotation, whereas yellow corresponds to clockwise rotation. (d) H–H′ lateral displacement profile across the left-lateral northeast-trending faults (N42°) in the fault-parallel component. (e) I–I′ lateral displacement profile across the right-lateral rupture (N140°) in the fault-parallel component. The color version of this figure is available only in the electronic edition.

fault did not reach the surface, and the deformation associated with dextral displacement shows up as a long-wavelength displacement gradient across the fault zone (Figs. 2a and 3a). A profile across that zone to measure the displacement in the direction parallel to the mainshock indicates that the total dextral displacement across the fault zone is ~1.5 m distributed over a zone ~2 km wide (Fig. 10e). In this northern part of the rupture zone, at least 15 northeast-trending faults were recognized based on the displacement discontinuities (Fig. 10a), indicating that they accommodated horizontal displacement. No vertical deformation could be measured across these faults (Fig. 3b), despite the fact that their orientation would be well suited for normal motion associated with the extensive Coso area. Instead, the curl map (Fig. 10c) shows that the displacement on these northeast-trending faults corresponds to left-lateral strike slip. This is consistent with their orientation, roughly parallel to the orientation of the foreshock. Measurement of the displacement in the direction parallel to these faults (Fig. 10d) reveals that each fault has accommodated between 0.1 and 0.5 m of left-lateral motion. However, taken together, the cumulative left-lateral displacement across the whole fault set is nearly zero (Fig. 10d), suggesting that this left-lateral motion is mostly related to individual block rotation inside the dextral shear zone corresponding to the northernmost extent of the mainshock rupture, following a bookshelf faulting pattern (Tapponnier *et al.*, 1990; Wesnousky, 2005).

Similar conclusions have been reached by Milliner *et al.* (2021) who used 6 m resolution horizontal displacement and strain maps to characterize the bookshelf faulting behavior. They propose bookshelf faulting to occur beyond fault tips to allow transitions between distinct right-lateral faults, as long as clockwise rotation and left-lateral shear are kinematically equivalent to regional dextral shear (Platt and Becker, 2013). In addition, we propose that bookshelf faulting can arise from the interaction between diffuse shear and preexisting structures in the crust, as it has also been suggested for the 1986 M_w 5.7 Mount Lewis earthquake (Kilb and Rubin, 2002). Indeed, the similarity in direction between the foreshock rupture (Fig. 2a) and the strike of relocated aftershocks clusters between 3 and 9 km depth (Ross *et al.*, 2019; Shelly, 2020) suggests that this northeast direction might correspond to some geological fabric affecting the basement at a regional scale. Although we do not have geological evidence of a predominant northeast-directed crustal fabric in the area, clusters of background seismicity with bimodal orientation (northeast and northwest) were evidenced in this region before the rupture (Fialko and Jin, 2021). However, the locations of these northeast-trending faults identified at the surface, with the exception of the foreshock rupture, do not directly correlate with the northeast-trending clusters of aftershocks at depth. Northeast-trending faults identified in this study are short (0.1–3 km) and located close by within specific deformation zones (Figs. 2a, 6, and 10). In contrast, the clusters of aftershocks are scattered all along the rupture.

At the northern end of the mainshock, the specific geometry of the northeast-trending cross faults might be indicative of the rupture process itself. Some of the faults have a curved geometry, whereas others have a sigmoidal shape with the northeastern part of the fault strands bent toward the south (northeast of the H–H′ profile in Fig. 10a), as illustrated by fault strands 2, 6, and 7 in Figure 10a. This is consistent with the deformation expected from dextral shear along the azimuth of the main rupture (N140°). It also implies that these cross faults were possibly activated either before or during the rupture period when the area went under dextral shear deformation. Although the main rupture did not reach to the surface, a possible scenario is that the dynamic stress pulse located ahead of the rupture propagating northward triggered motion along this preexisting fabric (Poliakov *et al.*, 2002; Vallage *et al.*, 2016; Okubo *et al.*, 2019) and led to the left-lateral displacement visible at the surface. In a second stage, these left-lateral fault strands were sheared right laterally, producing the sigmoid shape fractures visible in the displacement maps, as it has already been suggested for other events (Klinger *et al.*, 2005). Because the dextral fault never reached the surface, the sigmoid shape is still well preserved.

In the displacement maps, we can see that these faults are asymmetric with respect to the location of the right-lateral motion (Fig. 10a–c). The faults extend farther away on the northeastern side of the zone of dextral shear. The difference in length might be interpreted as a direct mechanical response of the medium to the location of the tensional lobe of the rupture on the eastern side of the northeast-trending fault system (Fig. 10a) in which opening of faults is facilitated (Kim *et al.*, 2004; Okubo *et al.*, 2019). This asymmetric pattern may be enhanced by the different mechanical response of the surficial sediments themselves, formed mainly by lacustrine and alluvium deposits to the east of the rupture, whereas the western side is formed by more indurated alluvial fan sediments and lake deposits overlying uplifted basement seating at shallow depth (Jennings *et al.*, 1962).

Comparison with kinematic slip inversions and implications for the rupture segmentation and the processes of surface deformation

We compare the distribution of slip at depth derived from several kinematic inversions compiled by Wang *et al.* (2020) to our surface displacements for the mainshock of the 2019 Ridgecrest sequence. In our study, we subdivided the rupture into three segments, bounded by variations in the rupture azimuth and geometrical complexities (Figs. 2a, 8b, and 9b). At depth, the estimations of fault-dip angle based on the relocated seismicity yield values ranging between 70° and 85° toward the southwest for the northern segment S1 (Ross *et al.*, 2019), and between 70° and 75° toward the northeast under the southern segment S3 (Ross *et al.*, 2019; Jin and Fialko, 2020; Plesch *et al.*, 2020). For the central segment of the rupture (S2), Plesch *et al.* (2020) inferred a 55° NE fault-dip angle for the primary fault plane (fault strand 5, Fig. 7a).

The predictions of the amount of slip at the surface derived from kinematic inversions are all in good agreement with our slip distribution at first order: maximum slip around the epicenter, linear decrease of slip toward the northern tip of the rupture, and constant slip south of the epicentral area until it dies out quickly (Fig. 11a). The model by Chen *et al.* (2020) is the only model that systematically underpredicts the surface slip by about 1 m along much of the rupture. It is also the only model that used teleseismic data in the inversion process, which might come at the expense of the characterization of the near-fault surface deformation. At depth, most of the models are characterized by three patches of large slip (Liu *et al.*, 2019; Chen *et al.*, 2020; Jin and Fialko, 2020; Wang *et al.*, 2020; Xu *et al.*, 2020). The solution from Wang *et al.* (2020) is presented in Figure 11b. Although the slip patch located to the south of the epicenter is well resolved, the separation between the slip patches associated, respectively, with the epicentral area and with the northern part of the rupture is less clear (Fig. 11b). These three slip patches are consistent with the rupture segmentation we proposed based on the surface rupture geometry and the surface-slip distribution (Figs. 8b and 9b). This observation supports work from Klinger (2010) that suggested some similarity between the characteristic length of the rupture segments (~15–25 km depending on the earthquake) and

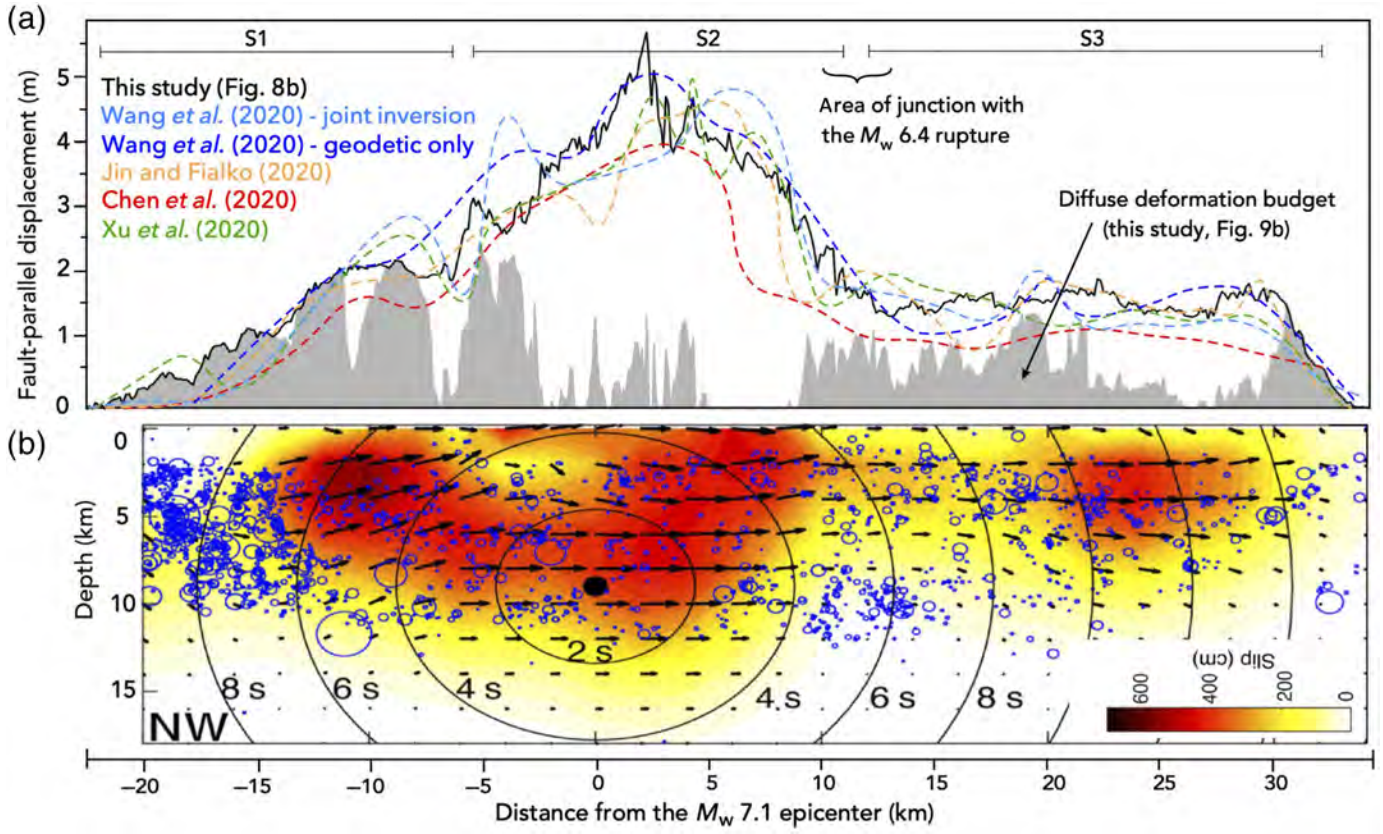

Figure 11. (a) Surface fault-parallel slip distribution along the mainshock rupture from this study in black (total displacement curve from Fig. 8b) and from five published kinematic inversions in color. For the models, predictions of slip on subparallel fault strands were added to obtain a total displacement prediction that is comparable to the displacement curve from this study (in black). Joint inversion from Wang *et al.* (2020) includes both seismic and geodetic data. Predictions of surface slip from the five kinematic inversions are projected onto a common line that follows the mean rupture azimuth (N140°), and values on subparallel fault strands are summed to obtain total surface displacement curves that are comparable with optical and field results from Figures 8b and 9b. Diffuse deformation calculated in this study (Fig. 9b) is shown in gray at the bottom. (b) Combined geodetic and seismological data inversion for the mainshock slip distribution on the primary fault plane from Wang *et al.* (2020). Slip vectors show relative motion of the east side of the kinematic fault model. Circular rupture front at a velocity of 2.2 km/s is in black. Blue circles are relocated aftershocks from Shelly (2020). The color version of this figure is available only in the electronic edition.

the size of peak-slip patches at depth. Hence, the segmentation of slip at depth for this earthquake seems to be a robust feature confirmed by most geophysical models (Fig. 11a) as well as by surface observations derived from both field- and optical-based measurements (Figs. 8b and 9b).

The area located between 10 and 20 km south of the epicenter, between subevents 2 and 3, shows limited slip at depth (Fig. 11b). At the surface, we measure lower fault slip and larger diffuse deformation, up to 50% of the total slip measured (Fig. 11a). This area of decreased slip is located just south of the M_w 6.4 left-lateral foreshock rupture. Coulomb stress models show that this area experienced a negative stress change of 1 MPa after the foreshock rupture (Wang *et al.*, 2020). The negative Coulomb stress change generated by the foreshock could have inhibited slip on the mainshock rupture but likely favored diffuse deformation in the surrounding medium as rocks are weaker under tension (Sammis *et al.*, 2009; Okubo *et al.*, 2019). The influence of the foreshock rupture on the mainshock displacement pattern could explain the sharp decrease in total surface displacement measured at the transition between segments 2 and 3 (Fig. 8b).

The fact that the kinematic models fit our data supports our strategy to measure surface deformation. Numerical models consider the bulk medium as elastic, so part of the diffuse deformation we measured using large-scale (>500 m) gradients might include some elastic deformation generated by subsurface fault-slip variations. However, without a modeling strategy that includes our near-fault data in the inversion process, we cannot quantify the amount of elastic versus inelastic deformation that occurred at the surface.

In attempt to qualitatively assess the importance of possible inelastic contribution, we predicted the elastic surface displacement associated with a blind rupture (Fig. 12). On the one hand, we used the results of the kinematic inversions as an input for our elastic model and compare the result with our displacement data. The fault extends from 1.5 km below the surface to 7 km

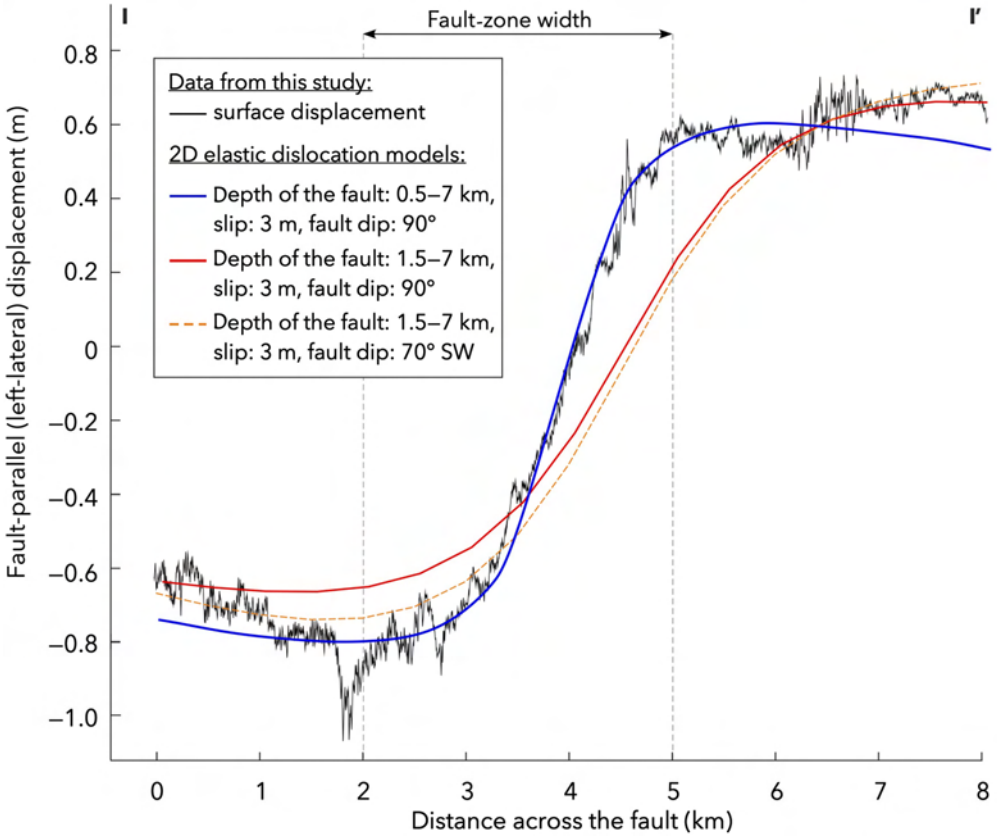

Figure 12. Displacement profile (black), in the fault-parallel component of displacement, taken across the diffuse deformation area to the north of the mainshock rupture (I–I′ profile from Fig. 10e). Predictions of surface displacements from 2D elastic models are presented in blue, red, and orange. Blue model corresponds to a direct fit of the data without data constraining the input parameters. Red and orange models use the kinematic slip models (Wang *et al.*, 2020) as input parameter. The fault is vertical in the red profile and dips 70°SW, similar to the geometry inferred from the distribution of aftershocks (Ross *et al.*, 2019) in the orange profile. The color version of this figure is available only in the electronic edition.

deep with a uniform slip of 3 m and dips either at 90° or at 70° SW (red and orange curves, Fig. 12). With this strategy, we could not fit the data in the near field, although amplitudes of the displacements away from the fault are similar. On the other hand, we directly fitted the data by assigning the fault at a depth of 500 m (blue curve, Fig. 12). In this case, although amplitudes of the displacements away from the fault do not correspond, we could fit the displacement gradient within the fault zone. Milliner *et al.* (2021) used this same strategy to fit the surface displacements 5 km to the southeast, still in the area of bookshelf faulting and diffuse deformation, and obtained results for a fault located 350 m below the surface. However, elastic strain of magnitudes as high as 10^{-3} and 10^{-4} (0.5%–0.05%) are unlikely to be accumulated over months within the last hundred meters of the crust (Postearthquake acquisitions occurred 1–2 months after the rupture, Table S1.) and would be released within the early postseismic phase (Brooks *et al.*, 2020; Wang and Bürgmann, 2020). So, it is likely that diffuse deformation represents inelastic permanent deformation.

FZW, spatial extent of the diffuse deformation, and SSD

In this study, we quantified the amount of diffuse deformation along the surface rupture of the M_w 7.1 mainshock Ridgecrest earthquake (31% of the total displacement budget, Fig. 9b). We showed that diffuse deformation is principally located along the northern and southern segments of the rupture (81% along S1 and 39% along S3). In contrast, in the central part of the rupture, which includes the epicentral region, we measured lower diffuse deformation (18%). The northern and southern areas are characterized by a significant SSD (Fialko *et al.*, 2005) according to the geophysical models (S1 and S3, Fig. 11b). Maximum slip at depth along S1 and S3 ranges between 4 and 6 m, whereas surface displacements reach a maximum of 2 m. Along these segments, strain distributes within the medium to accommodate the variations of fault slip toward the surface, generating diffuse deformation gradients at the surface. Using our observations only, we cannot quantify the part of deformation that is elastic and inelastic. However, we can measure the spatial extent of the surface deformation zone referred to as FZW (Fig. 13a and Fig. S9). This enables us to infer the volume of rock that is affected by diffuse deformation and determine the depth to which the SSD extends along the rupture.

The FZW is defined as the central area where deformation departs from the far-field gradients taken as references for the linear regressions on each side of the fault (Figs. 7a and 12). Along the mainshock surface rupture, the maximum FZW measured in our study reaches 4 km, and the mean FZW averages 2 km (Fig. 13a); thus, we measure deformation processes occurring within the first 2–4 km of the crust (Segall, 2010). Along the foreshock rupture, the FZW averages 680 m (Fig. S9). Hence, processes impacting the foreshock near-fault surface deformation patterns might occur at very shallow depths, likely a few hundred meters. Measurements of FZW from this study are compared with regional FZW reported

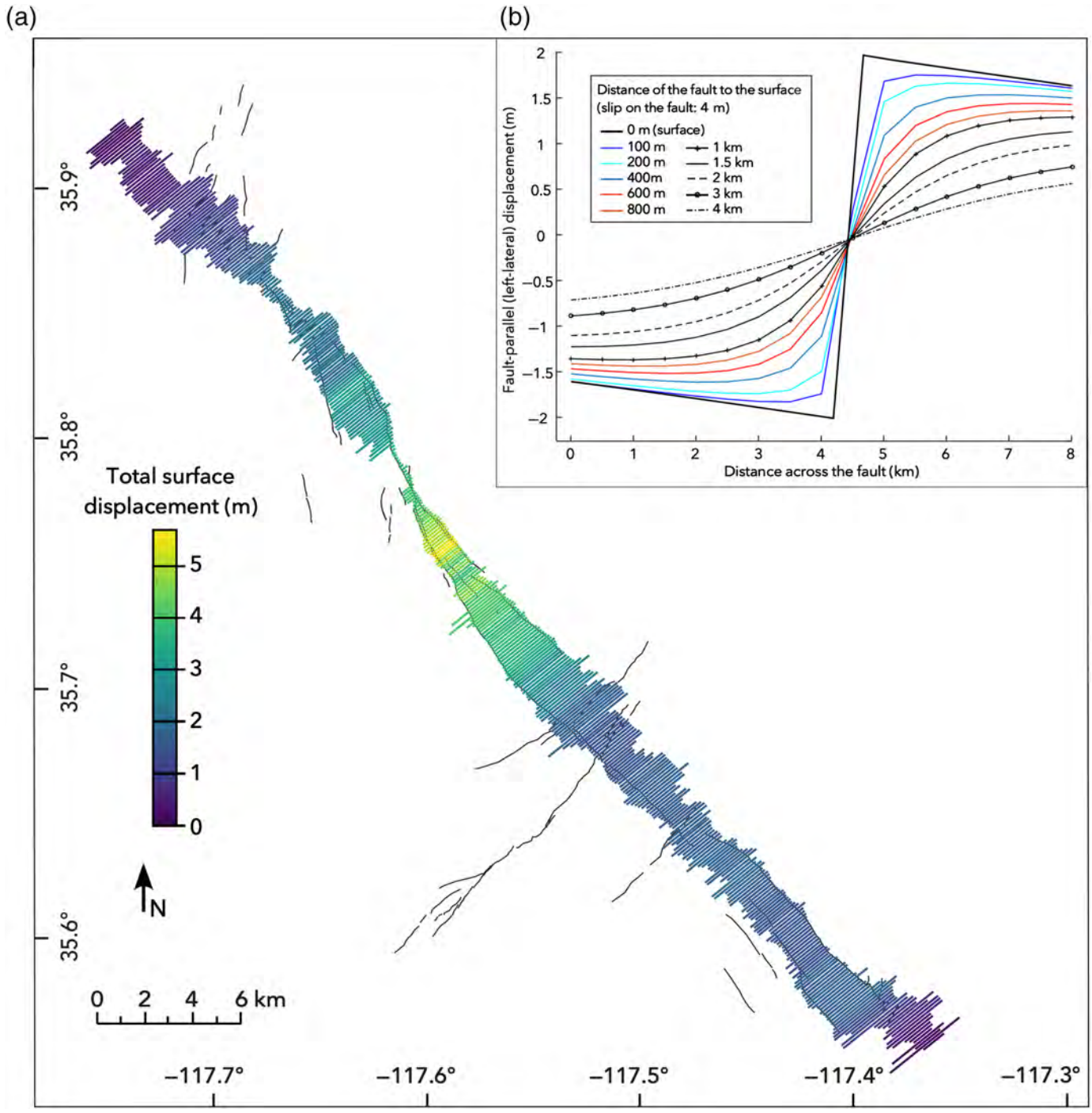

in Gold *et al.* (2021), in parallel with the total slip budget from this study (Fig. S10).

We use elastic modeling to infer the potential depth of the source of the displacements we image at the surface. We model surface displacements associated with a 4 m right-lateral strike-slip dislocation in an elastic medium (Fig. 13b). The bottom of the fault is fixed at 15 km depth, and the top of the fault is allowed to vary from 4 to 0 km, 0 km corresponding to a surface rupture. Using these simulations, we show that the wavelength of the surface elastic deformation associated with slip ending at a depth greater than a few kilometers is too long

Figure 13. (a) Map of the fault-zone width (FZW) along the mainshock surface rupture. Positions of the colored lines represent the western and eastern ends of the deformation zone in each of the 460 displacement profiles used to quantify slip along the mainshock rupture (e.g., Fig. 7a, vertical profile and Fig. S4). Colors represent the total displacement measured at each profile (Fig. 8b). Background map from DuRoss *et al.* (2020). FZW along the foreshock rupture is presented in Figure S9. (b) Surface displacement profiles for strike-slip motion on a vertical dislocation in an elastic medium. The upper limit of the dislocation varies from 0 to 4 km depth, and right-lateral slip is 4 m. The color version of this figure is available only in the electronic edition.

to significantly impact the amount of total displacement measured using 8 km long profiles. This confirms our suggestion that the deformation signal discussed here mostly relates to surficial deformation and does not result from elastic deformation associated with slip at large depths (>2 km).

New measurements presented in this study fill the gap between InSAR data, which image the regional displacement field and mostly bring information on fault slip at depth (>1–2 km depth), and field and optical data that focus on fault offsets and OFD at local scale (<500 m). In this study, we measured both a total displacement curve, which reflects slip at a shallow depth (<∼2 km), and a fault-slip curve that reflects localized fault deformation that reached the surface along the 20 fault strands that constitute the mainshock surface rupture. Diffuse deformation reflects the discrepancies between slip at shallow depth and surface slip. Hence, the fact that the kinematic slip predictions fit our data supports the existence of an SSD along segments 1 and 3 of the mainshock rupture. The presence of an SSD is consistent with the magnitude of the mainshock earthquake. Lauer *et al.* (2020) proposed that slip deficit on strike-slip faults most often occurred for earthquake of magnitudes lower than M_w 7.5, based on comparisons with slip models on various earthquakes and on the observation that no SSD was modeled for very large events such as the 2001 M_w 7.8 Kokoxili earthquake, the 2002 M_w 7.9 Denali earthquake, or the 2013 M_w 7.7 Baluchistan earthquake.

Similar to the mainshock surface rupture, we measured a mean diffuse deformation of 31% along the foreshock surface rupture (Fig. S7). This value of 31% of diffuse deformation differs greatly from the ∼59% and 56% of OFD measured, respectively, by Gold *et al.* (2021) and Milliner *et al.* (2021). This difference is mainly due to the fact that fault damage occurring in the 10–100 m around the fault is included within the localized fault-slip budget in our study. Hence, diffuse deformation measured in this study refers only to large-scale (>100 m) displacement gradients. Also, using our displacement maps, we could measure slip on a larger number of fault strands (Fig. S8) than those observed in the field. This leads to a smaller estimation of diffuse deformation for the foreshock rupture.

Apart from these considerations, we also observe that the FZW from the mainshock earthquake is not impacted by the transition from segments 2 to 3 and by the junction with the foreshock rupture (Fig. 13a). Continuity is observed in the FZW along the northeastern side of the fault zone from fault strands 16 to 19, which have a similar azimuth but are ∼10 km apart from each other. A similar observation is made along the southwestern side of the fault zone between fault strands 18 and 20 that are ∼7 km apart. Thus, it seems that the fault zone at depth is not impacted by the junction with the foreshock rupture. This supports our previous observation that the foreshock rupture is discontinuous across the mainshock, and that the mainshock rupture constitutes the major structure of the 2019 sequence and a barrier to the propagation of the foreshock rupture.

CONCLUSIONS

In this article, we presented a dataset of surface displacement measurements for the 2019 Ridgecrest, California, earthquake sequence, derived from correlation of 0.5 m resolution optical satellite images. We measured details of the surface displacements associated with both the foreshock and the mainshock earthquakes. This work highlights the respective importance of fault complexity and diffuse deformations in surface rupture processes. We show that slip measured in the field along primary surface ruptures underestimates the total amount of displacement. Diffuse deformations, which include both elastic and inelastic processes, can account for a significant part, up to 100%, of the total surface deformation in areas where the earthquake rupture barely reaches the surface. When considered along the entire length of the foreshock and mainshock ruptures, the diffuse deformation represents 31% of the total surface displacement budget. When considered together, localized deformation on small secondary faults also accommodate a significant part of the surface displacement budget, up to 50% in some areas of the rupture. The spatial distribution of the diffuse deformation and of the localized deformation on faults emphasizes lateral variations of the rupture process reflecting structural fault segmentation. These variations are primarily related to the geometry of the fault, which, in turn, depends on a fault's seismic history, the long-term evolution of the major geometrical complexities with cumulative slip, and interactions with preexisting structures from the geological fabric (Choi *et al.*, 2018; Lefevre *et al.*, 2018). Comparisons with other optical-based results and kinematic slip inversions enable us to corroborate the fact that SSD did occur along the foreshock and mainshock ruptures of the Ridgecrest sequence. This SSD affects the first ∼2 km of the crust and is responsible for part of the diffuse deformation we measured to the surface. However, it is not yet possible to discriminate with certainty between the elastic and inelastic contributions of the diffuse deformation using the currently available numerical models. On one side, inelastic deformation participates to the budget of finite deformation for this earthquake, and it must be taken into account when estimating the recurrence and future magnitudes of earthquakes in the area. It also indicates that deformation distributes over a wider area than what is directly visible to the surface. On the other side, if the deformation is elastic, it means that elastic strain has accumulated during the rupture, which should be released during the next seismic cycle.

DATA AND RESOURCES

The Pleiades images were provided by the Committee on Earth Observation Satellites (CEOS) Seismic Hazards Pilot from European Space Agency (ESA) (http://ceos.org/ourwork/workinggroups/disasters/earthquakes, last accessed September 2020) and the Incitation à l'utilisation scientifique des images Spot (ISIS) program from Centre national d'études spatiales (CNES) (https://dinamis.teledetection.fr, last accessed September 2020; https://cnes.fr, last accessed September 2020). The WorldView images (2019, DigitalGlobe/Maxar) were accessed via the

NextView licensing agreement. The Sentinel-2 images are freely available on scihub.copernicus.eu (last accessed September 2020). The U.S. Geological Survey Quaternary fault and fold database (Fig. 1) can be accessed at https://www.usgs.gov/natural-hazards/earthquake-hazards/faults (last accessed September 2020). Epicenter locations can be found at https://earthquake.usgs.gov (last accessed September 2020). The MATLAB available at www.mathworks.com/products/matlab (last accessed August 2021). Supplemental figures providing details on the methodology and on the results of this study are available in the supplemental materials. Surface displacement maps at 1 m ground resolution are available at S. L. Antoine, Y. Klinger, A. Delorme, K. Wang, R. Bürgmann, and R. D. Gold, 2021, "East-west, north-south and vertical displacement maps for the 2019 Ridgecrest earthquake sequence (California, USA) at 1 m ground resolution.", Mendeley Data, v1, doi: 10.17632/nj3khvs4yw.1.

DECLARATION OF COMPETING INTERESTS

The authors acknowledge that there are no conflicts of interest recorded.

ACKNOWLEDGMENTS

This work was partly supported by Terre solide, océan, surfaces continentales, atmosphère (TOSCA) CNES and by the ANR-18-CE31-0012 projects. Yann Klinger was supported by the Miller Foundation at UC Berkeley during his visit at UC Berkeley. This study contributed to the IdEx Université de Paris ANR-18-IDEX-0001. This is Institut du Physique du Globe de Paris (IPGP) Contribution 4234. Numerical computations were partly performed on the Service de Calcul Parallèle et de Traitement de Données en sciences de la Terre (S-CAPAD) platform, IPGP, France. The authors thank Chris Milliner, Nadine Reitman, an anonymous reviewer, Associate Editor, and guest editor Rui Chen for insightful comments that improved this article. Any use of trade, firm, or product names is for descriptive purposes only and does not imply endorsement by the U.S. Government.

REFERENCES

Allmendinger, R. W., N. Cardozo, and D. M. Fisher (2012). *Structural Geology Algorithms: Vectors and Tensors*, Cambridge University Press, 302 pp., doi: 10.1017/CBO9780511920202.

Barnhart, W. D., R. D. Gold, and J. Hollingsworth (2020). Localized fault-zone dilatancy and surface inelasticity of the 2019 Ridgecrest earthquakes, *Nature Geosci.* **13,** 699–704, doi: 10.1038/s41561-020-0628-8.

Biasi, G., and S. Wesnousky (2017). Bends and ends of surface ruptures, *Bull. Seismol. Soc. Am.* **107,** 2543–2560, doi: 10.1785/0120160292.

Brooks, B. A., S. E. Minson, C. L. Glennie, J. M. Nevitt, T. Dawson, R. Rubin, T. L. Ericksen, D. Lockner, K. Hudnut, V. Langenheim, *et al.* (2017). Buried shallow fault slip from the South Napa earthquake revealed by near-field geodesy, *Sci. Adv.* **3,** e1700525, doi: 10.1126/sciadv.1700525.

Brooks, B. A., J. Murray, J. Svarc, E. Phillips, R. Turner, M. Murray, T. Ericksen, K. Wang, S. Minson, R. Burgmann, *et al.* (2020). Rapid geodetic observations of spatiotemporally varying postseismic deformation following the Ridgecrest earthquake sequence: The U.S. Geological Survey response, *Seismol. Res. Lett.* **91,** 2108–2123, doi: 10.1785/0220200007.

Carlson, C. W., C. J. Pluhar, J. M. G. Glen, and M. J. Farner (2013). Kinematics of the west-central Walker Lane: Spatially and temporally variable rotations evident in the late Miocene Stanislaus Group, *Geosphere* **9,** 1530–1551, doi: 10.1130/GES00955.1.

Chen, K., J.-P. Avouac, S. Aati, C. Milliner, F. Zheng, and C. Shi (2020). Cascading and pulse-like ruptures during the 2019 Ridgecrest earthquakes in the Eastern California shear zone, *Nat. Comm.* **11,** Article Number 22, doi: 10.1038/s41467-019-13750-w.

Cheng, G., and W. D. Barnhart (2021). Permanent co-seismic deformation of the 2013 M_w 7.7 Baluchistan, Pakistan earthquake from high-resolution surface strain analysis, *J. Geophys. Res.* **126,** e2020JB020622, doi: 10.1029/2020JB020622.

Cheng, Y., and Y. Ben-Zion (2020). Variations of earthquake properties before, during, and after the 2019 M 7.1 Ridgecrest, CA, earthquake, *Geophys. Res. Lett.* **47,** e2020GL089650, doi: 10.1029/2020GL089650.

Choi, J., Y. Klinger, M. Ferry, J. Ritz, R. Kurtz, M. Rizza, L. Bollinger, B. Davaasambuu, N. Tsend-ayush, and S. Demberel (2018). Geologic inheritance and earthquake rupture processes: The 1905 M ≥ 8 Tsetserleg-Bulnay strike-slip earthquake sequence, Mongolia, *J. Geophys. Res.* **123,** 1925–1953, doi: 10.1002/2017JB013962.

Delorme, A., R. Grandin, Y. Klinger, M. Pierrot-Deseilligny, N. Feuillet, E. Jacques, E. Rupnik, and Y. Morishita (2020). Complex deformation at shallow depth during the 30 October 2016 M_w 6.5 Norcia earthquake: Interference between tectonic and gravity processes? *Tectonics* **39,** e2019TC005596, doi: 10.1029/2019TC005596.

Dolan, J. F., L. J. McAuliffe, E. J. Rhodes, S. F. McGill, and R. Zinke (2016). Extreme multi-millennial slip rate variations on the Garlock fault, California: Strain super-cycles, potentially time-variable fault strength, and implications for system-level earthquake occurrence, *Earth Planet. Sci. Lett.* **446,** 123–136, doi: 10.1016/j.epsl.2016.04.011.

DuRoss, C. B., R. D. Gold, T. E. Dawson, K. M. Scharer, K. J. Kendrick, S. O. Akciz, S. J. Angster, J. Bachhuber, S. Bacon, S. E. K. Bennett, *et al.* (2020). Surface displacement distributions for the July 2019 Ridgecrest, California, earthquake ruptures, *Bull. Seismol. Soc. Am.* **110,** 1400–1418, doi: 10.1785/0120200058.

DuRoss, C. B., S. F. Personius, A. J. Crone, S. S. Olig, M. D. Hylland, W. R. Lund, and D. P. Schwartz (2016). Fault segmentation: New concepts from the Wasatch fault zone, Utah, USA, *J. Geophys. Res.* **121,** 1131–1157, doi: 10.1002/2015JB012519.

Faulkner, D. R., T. M. Mitchell, E. Jensen, and J. Cembrano (2011). Scaling of fault damage zones with displacement and the implications for fault growth processes, *J. Geophys. Res.* **116,** no. B05403, doi: 10.1029/2010JB007788.

Fialko, Y., and Z. Jin (2021). Simple shear origin of the cross-faults ruptured in the 2019 Ridgecrest earthquake sequence, *Nature Geosci.* **14,** 513–518, doi: 10.1038/s41561-021-00758-5.

Fialko, Y., D. Sandwell, M. Simons, and P. Rosen (2005). Three-dimensional deformation caused by the Bam, Iran, earthquake and the origin of shallow slip deficit, *Nature* **435,** 295–299, doi: 10.1038/nature03425.

Fialko, Y., M. Simons, and D. Agnew (2001). The complete (3-D) surface displacement field in the epicentral area of the 1999 M_w 7.1 Hector Mine earthquake, California, from space geodetic observations, *Geophys. Res. Lett.* **28,** 3063–3066, doi: 10.1029/2001GL013174.

Fielding, E. J., Z. Liu, O. L. Stephenson, M. Zhong, C. Liang, A. Moore, S.-H. Yun, and M. Simons (2020). Surface deformation related to

the 2019 M_w 7.1 and 6.4 Ridgecrest earthquakes in California from GPS, SAR interferometry, and SAR pixel offsets, *Seismol. Res. Lett.* **91,** 2035–2046, doi: 10.1785/0220190302.

Finzi, Y., and S. Langer (2012). Predicting rupture arrests, rupture jumps and cascading earthquakes, *J. Geophys. Res.* **117,** no. B12303, doi: 10.1029/2012JB009544.

Floyd, M., G. Funning, Y. Fialko, R. Terry, and T. Herring (2020). Survey and continuous GNSS in the vicinity of the July 2019 Ridgecrest earthquakes, *Seismol. Res. Lett.* **91,** 2047–2054, doi: 10.1785/0220190324.

Fossen, H., R. A. Schultz, Z. K. Shipton, and K. Mair (2007). Deformation bands in sandstone: A review, *J. Geol. Soc.* **164,** 755–769, doi: 10.1144/0016-76492006-036.

Gan, W., J. L. Svarc, J. C. Savage, and W. H. Prescott (2000). Strain accumulation across the Eastern California shear zone at latitude 36°30′N, *J. Geophys. Res.* **105,** 16,229–16,236, doi: 10.1029/2000JB900105.

Gold, R. D., C. B. DuRoss, and W. D. Barnhart (2021). Coseismic surface displacement in the 2019 Ridgecrest earthquakes: Comparison of field measurements and optical image correlation results, *Geochem. Geophys. Geosys.* **22,** e2020GC009326, doi: 10.1029/2020GC009326.

Gold, R. D., N. G. Reitman, R. W. Briggs, W. D. Barnhart, G. P. Hayes, and E. Wilson (2015). On- and off-fault deformation associated with the September 2013 M_w 7.7 Balochistan earthquake: Implications for geologic slip rate measurements, *Tectonophysics* **660,** 65–78, doi: 10.1016/j.tecto.2015.08.019.

Griffith, W. A., S. Nielsen, G. D. Toro, and S. A. F. Smith (2010). Rough faults, distributed weakening, and off-fault deformation, *J. Geophys. Res.* **115,** no. B08409, doi: 10.1029/2009JB006925.

Haddon, E. K., C. B. Amos, O. Zielke, A. S. Jayko, and R. Bürgmann (2016). Surface slip during large Owens Valley earthquakes, *Geochem. Geophys. Geosys.* **17,** 2239–2269, doi: 10.1002/2015GC006033.

Hamiel, Y., V. Lyakhovsky, and A. Agnon (2004). Coupled evolution of damage and porosity in poroelastic media: Theory and applications to deformation of porous rocks, *Geophys. J. Int.* **156,** 701–713, doi: 10.1111/j.1365-246X.2004.02172.x.

Hauksson, E., K. Hutton, H. Kanamori, L. Jones, J. Mori, S. Hough, and G. Roquemore (1995). Preliminary report on the 1995 Ridgecrest earthquake sequence in eastern California, *Seismol. Res. Lett.* **66,** 54–60, doi: 10.1785/gssrl.66.6.54.

Huang, H., L. Meng, R. Bürgmann, W. Wang, and K. Wang (2020). Spatio-temporal foreshock evolution of the 2019 M 6.4 and M 7.1 Ridgecrest, California earthquakes, *Earth Planet. Sci. Lett.* **551,** 116582, doi: 10.1016/j.epsl.2020.116582.

Hudnut, K. W., L. Seeber, and J. Pacheco (1989). Cross-fault triggering in the November 1987 Superstition Hills earthquake sequence, southern California, *Geophys. Res. Lett.* **16,** 199–202, doi: 10.1029/GL016i002p00199.

Jennings, C. W., J. L. Burnett, and B. W. Troxel (1962). Geologic map of California: Trona sheet, California Division of Mines and Geology, Publication GAM023, 1:250,000.

Jin, Z., and Y. Fialko (2020). Finite slip models of the 2019 Ridgecrest earthquake sequence constrained by space geodetic data and aftershock locations, *Bull. Seismol. Soc. Am.* **110,** 1660–1679, doi: 10.1785/0120200060.

Jobe, J. A. T., B. Philibosian, C. Chupik, T. Dawson, S. E. K. Bennett, R. Gold, C. DuRoss, T. Ladinsky, K. Kendrick, E. Haddon, *et al.* (2020). Evidence of previous faulting along the 2019 Ridgecrest, California, earthquake ruptures, *Bull. Seismol. Soc. Am.* **110,** 1427–1456, doi: 10.1785/0120200041.

Kilb, D., and A. M. Rubin (2002). Implications of diverse fault orientations imaged in relocated aftershocks of the Mount Lewis, M_L 5.7, California, earthquake, *J. Geophys. Res.* **107,** 2294, ESE 5-1–ESE 5-17, doi: 10.1029/2001JB000149.

Kim, Y.-S., D. C. P. Peacock, and D. J. Sanderson (2004). Fault damage zones, *J. Struct. Geol.* **26,** 503–517, doi: 10.1016/j.jsg.2003.08.002.

King, G., and J. Nabelek (1985). Role of fault bends in the initiation and termination of earthquake rupture, *Science* **228,** 984–987, doi: 10.1126/science.228.4702.984.

Klinger, Y. (2010). Relation between continental strike-slip earthquake segmentation and thickness of the crust, *J. Geophys. Res.* **115,** no. B07306, doi: 10.1029/2009JB006550.

Klinger, Y., R. Michel, and G. King (2006). Evidence for an earthquake barrier model from $M_w \sim 7.8$ Kokoxili (Tibet) earthquake slip-distribution, *Earth Planet. Sci. Lett.* **242,** 354–364, doi: 10.1016/j.epsl.2005.12.003.

Klinger, Y., K. Okubo, A. Vallage, J. Champenois, A. Delorme, E. Rougier, Z. Lei, E. Knight, A. Munjiza, C. Satriano, *et al.* (2018). Earthquake damage patterns resolve complex rupture processes, *Geophys. Res. Lett.* **45,** 10,279–10,287, doi: 10.1029/2018GL078842.

Klinger, Y., X. Xu, P. Tapponnier, J. Van der Woerd, C. Lasserre, and G. King (2005). High-resolution satellite imagery mapping of the surface rupture and slip distribution of the M_w 7.8, 14 November 2001 Kokoxili earthquake, Kunlun fault, northern Tibet, China, *Bull. Seismol. Soc. Am.* **95,** 1970–1987, doi: 10.1785/0120040233.

Lauer, B., R. Grandin, and Y. Klinger (2020). Fault geometry and slip distribution of the 2013 M_w 7.7 Balochistan earthquake from inversions of SAR and optical data, *J. Geophys. Res.* **125,** e2019JB018380, doi: 10.1029/2019JB018380.

Lefevre, M., Y. Klinger, M. Al-Qaryouti, M. Le Béon, and K. Moumani (2018). Slip deficit and temporal clustering along the Dead Sea fault from paleoseismological investigations, *Sci. Rep.* **8,** Article Number 4511, doi: 10.1038/s41598-018-22627-9.

Leprince, S., S. Barbot, F. Ayoub, and J.-P. Avouac (2007). Automatic and precise orthorectification, coregistration, and subpixel correlation of satellite images, application to ground deformation measurements, *IEEE Trans. Geosci. Rem. Sens.* **45,** 1529–1558, doi: 10.1109/TGRS.2006.888937.

Liu, C., T. Lay, E. E. K. Brodsky Dascher-Cousineau, and X. Xiong (2019). Coseismic rupture process of the large 2019 Ridgecrest earthquakes from joint inversion of geodetic and seismological observations, *Geophys. Res. Lett.* **46,** 11,820–11,829, doi: 10.1029/2019GL084949.

Lockner, D. (1998). A generalized law for brittle deformation of Westerly granite, *J. Geophys. Res.* **103,** 5107–5123, doi: 10.1029/97JB03211.

Lozos, J. C., D. D. Oglesby, J. N. Brune, and K. B. Olsen (2012). Small intermediate fault segments can either aid or hinder rupture propagation at stepovers, *Geophys. Res. Lett.* **39,** L18305 , doi: 10.1029/2012GL053005.

Massonnet, D., M. Rossi, C. Carmona, F. Adragna, G. Peltzer, K. Feigl, and T. Rabaute (1993). The displacement field of the Landers earthquake mapped by radar interferometry, *Nature* **364,** 138–142, doi: 10.1038/364138a0.

McGill, S. F., and C. M. Rubin (1999). Surficial slip distribution on the central Emerson fault during the June 28, 1992, Landers earthquake, California, *J. Geophys. Res.* **104,** 4811–4833, doi: 10.1029/98JB01556.

Milliner, C., and A. Donnellan (2020). Using Planet Labs satellite imagery to separate the surface deformation between the 4 July M_w 6.4 foreshock and 5 July M_w 7.1 mainshock during the 2019 Ridgecrest earthquake sequence, *Seismol. Res. Lett.* **91,** 1986–1997, doi: 10.1785/0220190271.

Milliner, C., A. Donnellan, S. Aati, J.-P. Avouac, R. Zinke, J. F. Dolan, K. Wang, and R. Bürgmann (2021). Bookshelf kinematics and the effect of dilatation on fault zone inelastic deformation: Examples from optical image correlation measurements of the 2019 Ridgecrest earthquake sequence, *J. Geophys. Res.* **126,** e2020JB020551, doi: 10.1029/2020JB020551.

Milliner, C. W. D., J. F. Dolan, J. Hollingsworth, S. Leprince, and F. Ayoub (2016). Comparison of coseismic near-field and off-fault surface deformation patterns of the 1992 M_w 7.3 Landers and 1999 M_w 7.1 Hector Mine earthquakes: Implications for controls on the distribution of surface strain, *Geophys. Res. Lett.* **43,** 10,115–10,124, doi: 10.1002/2016GL069841.

Milliner, C. W. D., J. F. Dolan, J. Hollingsworth, S. Leprince, F. Ayoub, and C. G. Sammis (2015). Quantifying near-field and off-fault deformation patterns of the 1992 M_w 7.3 Landers earthquake, *Geochem. Geophys. Geosys.* **16,** 1577–1598, doi: 10.1002/2014GC005693.

Milliner, C. W. D., C. Sammis, A. A. Allam, J. F. Dolan, J. Hollingsworth, S. Leprince, and F. Ayoub (2016). Resolving fine-scale heterogeneity of co-seismic slip and the relation to fault structure, *Sci. Rep.* **6,** Article Number 27201, doi: 10.1038/srep27201.

Mitchell, T. M., and D. R. Faulkner (2009). The nature and origin of off-fault damage surrounding strike-slip fault zones with a wide range of displacements: A field study from the Atacama fault system, northern Chile, *J. Struct. Geol.* **31,** 802–816, doi: 10.1016/j.jsg.2009.05.002.

Nevitt, J. M., B. A. Brooks, R. D. Catchings, M. R. Goldman, T. L. Ericksen, and C. L. Glennie (2020). Mechanics of near-field deformation during co- and post-seismic shallow fault slip, *Sci. Rep.* **10,** Article Number 5031, doi: 10.1038/s41598-020-61400-9.

Okubo, K., H. S. Bhat, E. Rougier, S. Marty, A. Schubnel, Z. Lei, E. E. Knight, and Y. Klinger (2019). Dynamics, radiation, and overall energy budget of earthquake rupture with coseismic off-fault damage, *J. Geophys. Res.* **124,** 11,771–11,801, doi: 10.1029/2019JB017304.

Peltzer, G., F. Crampé, S. Hensley, and P. Rosen (2001). Transient strain accumulation and fault interaction in the Eastern California shear zone, *Geology* **29,** 975–978, doi: 10.1130/0091-7613(2001)029<0975:TSAAFI>2.0.CO;2.

Petersen, M. D., and S. G. Wesnousky (1994). Fault slip rates and earthquake histories for active faults in southern California, *Bull. Seismol. Soc. Am.* **84,** 1608–1649.

Platt, J. P., and T. W. Becker (2013). Kinematics of rotating panels of E–W faults in the San Andreas system: What can we tell from geodesy? *Geophys. J. Int.* **194,** 1295–1301, doi: 10.1093/gji/ggt189.

Plesch, A., J. H. Shaw, Z. E. Ross, and E. Hauksson (2020). Detailed 3D fault representations for the 2019 Ridgecrest, California, earthquake sequence, *Bull. Seismol. Soc. Am.* **110,** 1818–1831, doi: 10.1785/0120200053.

Poliakov, A. N. B., R. Dmowska, and J. R. Rice (2002). Dynamic shear rupture interactions with fault bends and off-axis secondary faulting, *J. Geophys. Res.* **107,** no. B11, ESE 6-1-ESE 6-18, doi: 10.1029/2001JB000572.

Ponti, D., J. Blair, C. Rosa, K. Thomas, A. Pickering, S. Akciz, S. Angster, J.-P. Avouac, J. Bachhuber, S. Bacon, *et al.* (2020). Documentation of surface fault rupture and ground-deformation features produced by the 4 and 5 July 2019 M_w 6.4 and M_w 7.1 Ridgecrest earthquake sequence, *Seismol. Res. Lett.* **91,** 2942–2959, doi: 10.1785/0220190322.

Qiu, Q., S. Barbot, T. Wang, and S. Wei (2020). Slip complementarity and triggering between the foreshock, mainshock, and afterslip of the 2019 Ridgecrest rupture sequence, *Bull. Seismol. Soc. Am.* **110,** 1701–1715, doi: 10.1785/0120200037.

Ramsay, J. G. (1967). *Folding and Fracturing of Rocks*, McGraw-Hill, New York, New York, 568 pp.

Rockwell, T. K., and Y. Klinger (2013). Surface rupture and slip distribution of the 1940 Imperial Valley earthquake, Imperial fault, southern California: Implications for rupture segmentation and dynamics, *Bull. Seismol. Soc. Am.* **103,** 629–640, doi: 10.1785/0120120192.

Rockwell, T. K., S. Lindvall, T. Dawson, R. Langridge, W. Lettis, and Y. Klinger (2002). Lateral offsets on surveyed cultural features resulting from the 1999 Izmit and Düzce earthquakes, Turkey, *Bull. Seismol. Soc. Am.* **92,** 79–94, doi: 10.1785/0120000809.

Roquemore, G. (1980). Structure, tectonics, and stress field of the Coso Range, Inyo County, California, *J. Geophys. Res.* **85,** 2434–2440, doi: 10.1029/JB085iB05p02434.

Ross, Z. E., B. Idini, Z. Jia, O. L. Stephenson, M. Zhong, X. Wang, Z. Zhan, M. Simons, E. J. Fielding, S.-H. Yun, *et al.* (2019). Hierarchical interlocked orthogonal faulting in the 2019 Ridgecrest earthquake sequence, *Science* **366,** 346–351, doi: 10.1126/science.aaz0109.

Rosu, A.-M., M. Pierrot-Deseilligny, A. Delorme, R. Binet, and Y. Klinger (2015). Measurement of ground displacement from optical satellite image correlation using the free open-source software MicMac, special issue, *ISPRS J. Photogramm. Rem. Sens.* **100,** 48–59, doi: 10.1016/j.isprsjprs.2014.03.002.

Rupnik, E., M. Daakir, and M. P. Deseilligny (2017). MicMac—A free, open-source solution for photogrammetry, *Open Geospat. Data Softw. Stand.* **2,** Article Number 14, doi: 10.1186/s40965-017-0027-2.

Rupnik, E., M. P. Deseilligny, A. Delorme, and Y. Klinger (2016). Refined satellite image orientation in the free open-source photogrammetric tools Apero/MicMac, *ISPRS Ann. Photogramm. Rem. Sens.* **3,** 83–90, doi: 10.5194/isprsannals-III-1-83-2016.

Rupnik, E., M. Pierrot-Deseilligny, and A. Delorme (2018). 3D reconstruction from multi-view VHR-satellite images in MicMac, *ISPRS J. Photogramm. Rem. Sens.* **139,** 201–211, doi: 10.1016/j.isprsjprs.2018.03.016.

Sammis, C., A. Rosakis, and H. Bhat (2009). Effects of off-fault damage on earthquake rupture propagation: Experimental studies, in *Mechanics, Structure and Evolution of Fault Zones*,Y. Ben-Zion and C. Sammis (Editors), Pageoph Topical Volumes, Birkhäuser, Basel, Switzerland, 1629–1648, doi: 10.1007/978-3-0346-0138-2_5.

Schwartz, D., and K. Coppersmith (1984). Fault behavior and characteristic earthquakes: Examples from the Wasatch and San Andreas fault zones, *J. Geophys. Res.* **89,** 5681–5698, doi: 10.1029/JB089iB07p05681.

Segall, P. (2010). *Earthquake and Volcano Deformation*, STU-Student Edition, Princeton University Press, 456 pp.

Shelef, E., and M. Oskin (2010). Deformation processes adjacent to active faults: Examples from eastern California, *J. Geophys. Res.* **115,** no. B05308, doi: 10.1029/2009JB006289.

Shelly, D. R. (2020). A high-resolution seismic catalog for the initial 2019 Ridgecrest earthquake sequence: Foreshocks, aftershocks, and faulting complexity, *Seismol. Res. Lett.* **91,** 1971–1978, doi: 10.1785/0220190309.

Sieh, K., L. Jones, E. Hauksson, K. Hudnut, D. Eberhart-Phillips, T. Heaton, S. Hough, K. Hutton, H. Kanamori, A. Lilje, *et al.* (1993). Near-field investigations of the Landers earthquake sequence, April to July 1992, *Science* **260,** 171–176, doi: 10.1126/science.260.5105.171.

Tapponnier, P., R. Armijo, I. Manighetti, and V. Courtillot (1990). Bookshelf faulting and horizontal block rotations between overlapping rifts in southern Afar, *Geophys. Res. Lett.* **17,** 1–4, doi: 10.1029/GL017i001p00001.

Tchalenko, J. S., and N. Ambraseys (1970). Structural analysis of the Dasht-e Bayaz (Iran) earthquake fractures, *Geol. Soc. Am. Bull.* **81,** 41–60, doi: 10.1130/0016-7606(1970)81[41:SAOTDB]2.0.CO;2.

ten Brink, U. S., N. C. Miller, B. D. Andrews, D. S. Brothers, and P. J. Haeussler (2018). Deformation of the Pacific/North America plate boundary at Queen Charlotte fault: The possible role of rheology, *J. Geophys. Res.* **123,** 4223–4242, doi: 10.1002/2017JB014770.

Treiman, J. A., K. J. Kendrick, W. A. Bryant, T. K. Rockwell, and S. F. McGill (2002). Primary surface rupture associated with the M_w 7.1 16 October 1999 Hector Mine earthquake, San Bernardino County, California, *Bull. Seismol. Soc. Am.* **92,** 1171–1191, doi: 10.1785/0120000923.

Vallage, A., Y. Klinger, R. Grandin, H. S. Bhat, and M. Pierrot-Deseilligny (2015). Inelastic surface deformation during the 2013 M_w 7.7 Balochistan, Pakistan, earthquake, *Geology* **43,** 1079–1082, doi: 10.1130/G37290.1.

Vallage, A., Y. Klinger, R. Lacassin, A. Delorme, and M. Pierrot-Deseilligny (2016). Geological structures control on earthquake ruptures: The M_w 7.7, 2013, Balochistan earthquake, Pakistan: Geological control on earthquake, *Geophys. Res. Lett.* **43,** 10,155–10,163, doi: 10.1002/2016GL070418.

Wang, K., and R. Bürgmann (2020). Co- and early postseismic deformation due to the 2019 Ridgecrest earthquake sequence constrained by Sentinel-1 and COSMO-SkyMed SAR data, *Seismol. Res. Lett.* **91,** 1998–2009, doi: 10.1785/0220190299.

Wang, K., D. Dreger, E. Tinti, R. Burgmann, and T. Taira (2020). Rupture process of the 2019 Ridgecrest, California M_w 6.4 foreshock and M_w 7.1 earthquake constrained by seismic and geodetic data, *Bull. Seismol. Soc. Am.* **110,** 1603–1626, doi: 10.1785/0120200108.

Wesnousky, S. G. (2005). Active faulting in the Walker Lane, *Tectonics* **24,** TC3009, doi: 10.1029/2004TC001645.

Willis, M. J., W. D. Barnhart, R. Cassotto, J. Klassen, J. Corcoran, T. Host, B. Huberty, K. Pelletier, and J. F. Knight (2019). CaliDEM: Ridgecrest, CA region 2m digital surface elevation model, Funding by NSF and USGS, Data collection by DigitalGlobe, Distributed by OpenTopography, doi: 10.5069/G998854C.

Xu, X., D. T. Sandwell, and B. Smith-Konter (2020). Coseismic displacements and surface fractures from Sentinel-1 InSAR: 2019 Ridgecrest earthquakes, *Seismol. Res. Lett.* **91,** 1979–1985, doi: 10.1785/0220190275.

Zhou, Y., B. E. Parsons, and R. T. Walker (2018). Characterizing complex surface ruptures in the 2013 M_w 7.7 Balochistan earthquake using three-dimensional displacements, *J. Geophys. Res.* **123,** 10,191–10,211, doi: 10.1029/2018JB016043.

Zimmaro, P., C. C. Nweke, J. L. Hernandez, K. S. Hudson, M. B. Hudson, S. K. Ahdi, M. L. Boggs, C. A. Davis, C. A. Goulet, S. J. Brandenberg, *et al.* (2020). Liquefaction and related ground failure from July 2019 Ridgecrest earthquake sequence, *Bull. Seismol. Soc. Am.* **110,** 1549–1566, doi: 10.1785/0120200025.

Zinke, R., J. Hollingsworth, and J. F. Dolan (2014). Surface slip and off-fault deformation patterns in the 2013 M_w 7.7 Balochistan, Pakistan earthquake: Implications for controls on the distribution of near-surface coseismic slip, *Geochem. Geophys. Geosys.* **15,** 5034–5050, doi: 10.1002/2014GC005538.

Zinke, R., J. Hollingsworth, J. F. Dolan, and R. V. Dissen (2019). Three-dimensional surface deformation in the 2016 M_w 7.8 Kaikōura, New Zealand, earthquake from optical image correlation: Implications for strain localization and long-term evolution of the Pacific-Australian plate boundary, *Geochem. Geophys. Geosys.* **20,** 1609–1628, doi: 10.1029/2018GC007951.

Manuscript received 15 February 2021